Multi-Size-Mesh, Multi-Time-Step Algorithm for Noise Computation on Curvilinear Meshes

Thomas Le Garrec, Xavier Gloerfelt, Christophe Eric Corre

HAL Id: hal-01069756

https://hal.science/hal-01069756

Submitted on 29 Sep 2014

To cite this version :

Multi-Size-Mesh, Multi-Time-Step Algorithm for Noise Computation on Curvilinear Meshes

T. Le Garrec[1†], X. Gloerfelt[1*], C. Corre[2]

[1] *DynFluid Laboratory - Arts et Métiers ParisTech , 75013 Paris, France;* [2] *LEGI Laboratory - BP 53, 38041 Grenoble Cedex 9, France*

SUMMARY

Aeroacoustic problems are often multiscale and a zonal refinement technique is thus desirable to reduce computational effort while preserving low dissipation and low dispersion errors from the numerical scheme. For that purpose, the multi-size-mesh, multi-time-step algorithm of Tam and Kurbatskii [*AIAA Journal*, 2000, **38**(8), p. 1331-1339] allows changes by a factor of two between adjacent blocks, accompanied by a doubling in the time step. This local time stepping avoids wasting calculation time which would result from imposing a unique time step dictated by the smallest grid size for explicit time marching. In the present study, the multi-size-mesh, multi-time-step method is extended to general curvilinear grids by using a suitable coordinate transformation and by performing the necessary interpolations directly in the physical space thanks to multidimensional interpolations combining order constraints and optimization in the wavenumber space. A particular attention is paid to the properties of the Adams-Bashforth schemes used for time marching. The optimization of the coefficients by minimizing an error in the wavenumber space rather than statisfying a formal order is shown to be inefficient for Adams-Bashforth schemes. The accuracy of the extended multi-size-mesh, multi-time-step algorithm is first demonstrated for acoustic propagation on a sinusoidal grid and for a computation of laminar trailing edge noise. In the latter test-case, the mesh doubling is close to the airfoil and the vortical structures are crossing the doubling interface without affecting the quality of the radiated field. The applicability of the algorithm in 3D is eventually demonstrated by computing tonal noise from a moderate-Reynolds-number flow over an airfoil. Copyright © 2012 John Wiley & Sons, Ltd.

1. INTRODUCTION

With the rapid advances in computational methodology, turbulence modeling and the availability of fast computers, noise investigations by Direct Noise Computation (DNC) [*i.e.* simulation of aerodynamic and acoustic quantities in the same run] are made possible. The main difficulty

---

*Correspondence to: DynFluid Laboratory, Arts et Métiers ParisTech, 151 boulevard de l'Hôpital, 75013 Paris, France, E-mail: xavier.gloerfelt@paris.ensam.fr.
†Present address: ONERA, The French Aerospace Lab, 92322 Chatillon cedex, France.

of such simulations comes from the large disparities between the fine scales of turbulence and the large wavelengths of acoustic radiation which impose severe constraints on the meshes. In Computational Aeroacoustics (CAA), the preservation of the weak propagative waves with the turbulent motions can be achieved through the use of high-order finite differences in conjunction with structured meshes [1]. Local refinement is hardly achievable, and can lead to unacceptable grid sizes. The use of unstructured meshes, in conjunction with Discontinuous Galerkin method for instance [2], could be an alternative, but would still induce a significant computational cost. Another attempt to preserve a high accuracy on structured or unstructured grids consists in the extension of the finite difference schemes in the finite volume context. Gaitonde and Shang [3] propose the use of 4th-order compact finite volume schemes. An implicit deconvolution step relates cell averaged values to face values. The development of high-order compact deconvolution schemes is described by Kobayashi [4]. Pereira and Kobayashi [5] discussed the implementation for the incompressible Navier-Stokes equations. This strategy is pursued by Lacor *et al.* [6], who developed a multidimensional compact deconvolution for application to arbitrary meshes. In the compressible regime, Popescu *et al.* [7] propose to extend directly Dispersion-Relation-Preserving (DRP) or optimized prefactored scheme in the finite volume context. The high-order accuracy is obtained however at the price of an important extra cost. The Adaptative Mesh Refinement (AMR) method introduced by Berger and Oliger [8], or Roger and Colella [9] in the framework of Cartesian grids, allows local grid refinements but proves difficult to apply with high-order spatial schemes. Moreover difficulties occur when the geometry is not Cartesian. Steinthorsson *et al.* [10] present an extension of the AMR technique for structured body fitted grids by using Hermite interpolations to generate the grid. The use of multi-grid or zonal grid technique is also commonly recognized as a useful method to increase the computational efficiency. The use of zonal grids has started with applications in meteorology, oceanography and atmospheric boundary layers and has then been used for turbulence simulations by DNS [11]; it has developed following two main strategies which are briefly reviewed to provide a non-exhaustive panorama of this rapidly expanding field.

In the first strategy, the grids can be generated independently for different zones or components and the grid overlap is allowed. Different zones or blocks get their boundary data using interpolation from neighboring blocks. Historically, the overset methods, also referred to as chimera methods, have been developed in the eighties by Benek *et al.* [12] or Steger *et al.* [13]. In the framework of CAA applications, Desquesnes *et al.* [14] proposed high-order overlapping grid method for coupling CFD and CAA; Sherer and Scott [15], Chicheportiche and Gloerfelt [16], or Daude *et al.* [17] considered many different interpolation techniques in order to determine the most accurate and robust ones for a wide range of applications.

In the second strategy, the mesh is generated by successive refinements at different grid levels, where the coarse grid solution is used as a boundary condition for the next finer grid level. The main drawback of this strategy is that without a coupling of the fine grid and coarse grid solutions, it will only provide coarse grid accuracy at the interfaces and will lead to some distorsions at the grid interfaces. Therefore, a special treatment has to be developed for the interface. In most of the cases, a high-order interpolation procedure for exchanging information between zones and a special treatment of the points near the interface are developed. Manhart [18] proposed a zonal method

with a second-order finite volume formulation. Kravchenko *et al.* [11] use spectral interpolations based on B-splines. In the present work, the multi-size-mesh multi-time-step strategy introduced by Tam and Kurbatskii [19, 20, 21] is followed: a doubling in the mesh size is accompanied by a doubling in the time step. The partitioning of the whole calculation domain allows local refinements and the number of grid points can thus be reduced. Tam and Kurbatskii [19] have considered Cartesian grids in their work. This method has been applied by Yin and Delfs [22] to rotor noise using a multi-domain Cartesian grid without the corresponding doubling of the time step. Tam and Ju [23] used both changes in the mesh size and time step in curvilinear meshes by working directly in the transformed elliptic coordinates. The use of a local time stepping alone has also been proposed. Allampalli and Hixon [24] used multi-time-step Adams-Bashforth schemes, in which different regions of the computational domain are made to march in time with different time steps. The multi-time-step strategy of Lin *et al.* [25] is designed for overset grids. No constraint is imposed on the ratio of mesh sizes between neighboring blocks thanks to a time interpolation used in the vicinity of the interface. Lörcher *et al.* [26] propose to define a local time step for each cell of a Discontinous Galerkin method. The communication with neighbouring cells is ensured by solving a Cauchy-Kowalewski equation.
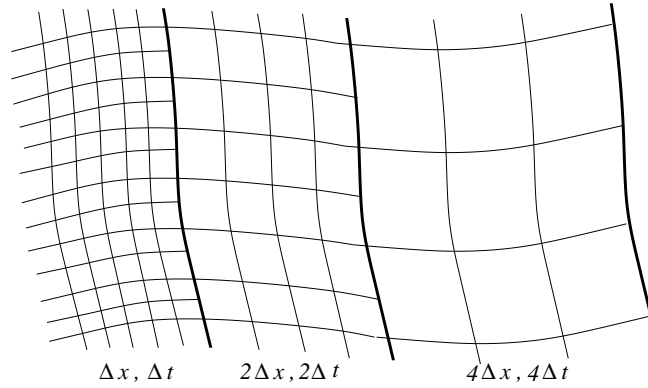

Figure 1. Changing in the mesh size and in the time step between three blocks.

In the present study, the multi-size-mesh, multi-time-step algorithm of Tam and Kurbatskii [20] is extended to general curvilinear grids by using a suitable coordinate transform and multidimensional interpolation directly in the curvilinear space. In the example of trailing edge noise from an airfoil, the local adaptation of the mesh size and of the time step can significantly reduce the computational effort. The numerical algorithm is presented in section 2, where discretization schemes on an 11-point stencils are derived for points near the doubling interface. The suitability of combining order constraints and optimization in the wavenumber space when deriving multidimensional interpolation coefficients is underlined. In section 3, a particular attention is devoted to the stability and accuracy properties of Adams-Bashforth schemes which are selected for time marching. Their efficiency is compared to Runge-Kutta methods. A first test-case for wave propagation is tackled in section 4 to check that the accuracy is preserved on sinusoidal grids. Laminar trailing edge noise from the flow over a NACA0012 airfoil at a Reynolds number based on the chord of Re_c=5000 is used as a benchmark for the method in section 5. Finally, a three-dimensional example is given in

section 6 for the flow over a NACA0018 with an incidence of 6° and Re$_c$=160 000, where tonal noise is expected.

2. NUMERICAL ALGORITHM

2.1. *Governing equations*

The compressible Navier-Stokes equations are solved in conservative form as

$$\frac{\partial \mathbf{U}}{\partial t} + \frac{\partial}{\partial x}(\mathbf{F_e} - \mathbf{F_v}) + \frac{\partial}{\partial y}(\mathbf{G_e} - \mathbf{G_v}) = 0$$

where $\mathbf{U} = (\rho, \rho u, \rho v, \rho E)^{\mathrm{T}}$ is the vector of unknowns. The inviscid (subscript **e**) and visco-thermal fluxes (subscript **v**) are given by:

$$\mathbf{F_e} = \left(\rho u, \rho u^2 + p, \rho uv, (\rho E + p)u\right)^{\mathrm{T}} \; ; \quad \mathbf{F_v} = \left(0, \tau_{xx}, \tau_{xy}, u\tau_{xx} + v\tau_{xy} - q_x\right)^{\mathrm{T}}$$

$$\mathbf{G_e} = \left(\rho v, \rho uv, \rho v^2 + p, (\rho E + p)v\right)^{\mathrm{T}} \; ; \quad \mathbf{G_v} = \left(0, \tau_{xy}, \tau_{yy}, u\tau_{xy} + v\tau_{yy} - q_y\right)^{\mathrm{T}}$$

For an ideal gas, the specific total energy E is defined as

$$E = p/[(\gamma - 1)\rho] + (u^2 + v^2)/2, \quad \text{and} \quad p = \rho r T,$$

where T is the temperature, r the gas constant, and γ the ratio of specific heats. The viscous stress tensor τ_{ij} is modeled as a Newtonian fluid $\tau_{ij} = 2\mu S_{ij} - (2/3)\mu S_{kk}\delta_{ij}$, where $S_{ij} = (u_{i,j} + u_{j,i})/2$ is the rate of strain tensor. Here μ is the dynamic molecular viscosity, approximated with Sutherland's law:

$$\mu(T) = \mu_0 \left(\frac{T}{T_0}\right)^{\frac{3}{2}} \frac{T_0 + 110.4}{T + 110.4}$$

with T_0=273.15 K and μ_0=1.711×10^5 kg.m^{-1}.s^{-1}. The heat flux component q_α models thermal conduction in the α-direction with Fourier's law $q_\alpha = -(\mu c_p/\mathrm{Pr})(\partial T/\partial x_\alpha)$, where Pr=0.72 is the Prandtl number, and c_p is the specific heat at constant pressure.

The physical space (x,y) is mapped into a Cartesian regular computational space (ξ,η) thanks to coordinate transform. Consequently, large-stencil finite-difference schemes can easily be applied. The geometrical mapping is characterized by its Jacobian matrix:

$$J = \begin{vmatrix} \dfrac{\partial \xi}{\partial x} & \dfrac{\partial \eta}{\partial x} \\ \dfrac{\partial \xi}{\partial y} & \dfrac{\partial \eta}{\partial y} \end{vmatrix} = \begin{vmatrix} \xi_x & \eta_x \\ \xi_y & \eta_y \end{vmatrix} \tag{1}$$

The transformed equations can be written as follows [27, 28]:

$$\frac{\partial}{\partial t}\left(\frac{\mathbf{U}}{J}\right) + \frac{\partial}{\partial \xi}\left(\frac{1}{J}(\xi_x(\mathbf{F_e} - \mathbf{F_v}) + \xi_y(\mathbf{G_e} - \mathbf{G_v}))\right) + \frac{\partial}{\partial \eta}\left(\frac{1}{J}(\eta_x(\mathbf{F_e} - \mathbf{F_v}) + \eta_y(\mathbf{G_e} - \mathbf{G_v}))\right) = 0$$

2.2. *Specific centered finite-difference schemes*

The 11-point centered optimized finite difference scheme of Bogey and Bailly [29] is used for approximating spatial derivatives at the interior points. The choice of an 11-point stencil scheme optimized in the wavenumber space has been proven to be a good trade-off in term of efficiency for wave propagation phenomena [29], and for large-eddy simulations of developed turbulence [30]. Furthermore, the explicit character of the scheme is well-suited to design special stencils for the mesh doubling. Indeed, when the grid size is double between two adjacent blocks as in Figure 1, five points of the fine block near the doubling interface require a particular treatment. The idea suggested by Tam and Kurbatskii [20, 21] consists in building special stencils in order to keep centered schemes. The straightforward extension to an 11-point stencil is presented in Figure 2. The five points located in the interface of the coarse block are easily dealt with by taking every two point of the fine block. Coefficients for 13- or 15-point stencils are given by Tam [21]. Note that other stencils could be considered, such as non-centered stencils [31], which introduce an additional dissipative error.
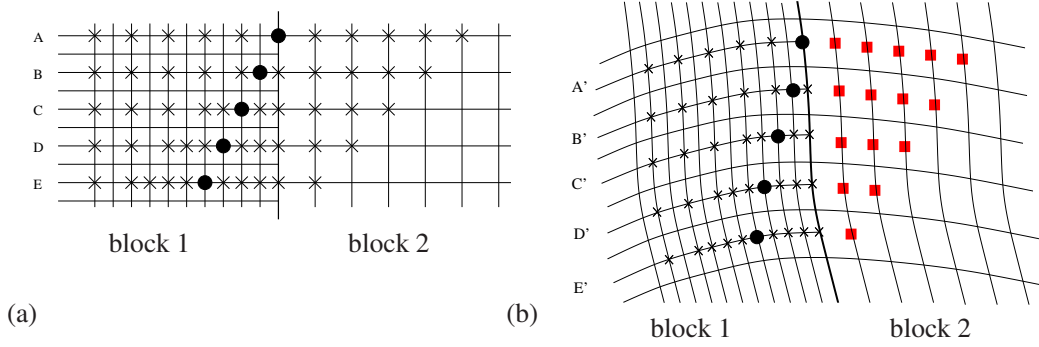

Figure 2. Buffer region between Δx and $2\Delta x$ blocks, and specific centered stencils: (●) application point, (×) stencil. (a) The scheme is applied in the regular Cartesian computational space. (b) For the stencils at points A',B',C',D',E', the missing values represented by a red square (■) have to be interpolated.

At point B in Figure 2(a), for instance, the first-order derivative $(\partial f/\partial x)_B$ is approximated by:

$$\left(\frac{\partial f}{\partial x}\right)_B = \frac{1}{\Delta x}\sum_{j=1}^{5} a_j^B \left(f_j^B - f_{-j}^B\right) \tag{2}$$

where

$$f_{-j}^B = f(x_B - \Delta_{|j|}^B x) \qquad j\text{=-5,..,-1}$$
$$f_j^B = f(x_B + \Delta_j^B x) \qquad j\text{=1,..,5} \tag{3}$$
$$\Delta_1^B x = \Delta x, \quad \Delta_2^B x = 3\Delta x, \quad \Delta_3^B x = 5\Delta x, \quad \Delta_4^B x = 7\Delta x, \quad \Delta_5^B x = 9\Delta x \tag{4}$$

Following the DRP concept, the centered schemes are designed to minimize the dispersion error. The effective wavenumber $k^\star$ of the scheme is obtained by applying a spatial Fourier transform to Equation (2):

$$k^\star \Delta x = \sum_{j=1}^{5} a_j^B \sin\left(k\Delta_j^B x\right) \tag{5}$$

The coefficients a_j^B for an optimized scheme of order 4 on an 11-point stencil are calculated by satisfying the two first relationships canceling the terms of the Taylor expansions up to Δx^4 and by adding three relationships $\partial E/\partial a_j^B = 0$ for $1 \leq j \leq 3$. The dispersion error E is defined as [29]:

$$E = \int_{\ln(k\Delta x)_l}^{\ln(k\Delta x)_h} |k^\star \Delta x - k\Delta x| \, d(\ln(k\Delta x))$$

where $\ln(k\Delta x)_l = \pi/16$ and $\ln(k\Delta x)_h = \pi/2$ are chosen.

The same method is applied for points C, D and E with:

$$\begin{cases} \Delta_1^C x = \Delta x, & \Delta_2^C x = 2\Delta x, & \Delta_3^C x = 4\Delta x, & \Delta_4^C x = 6\Delta x, & \Delta_5^C x = 8\Delta x \\ \Delta_1^D x = \Delta x, & \Delta_2^D x = 2\Delta x, & \Delta_3^D x = 3\Delta x, & \Delta_4^D x = 5\Delta x, & \Delta_5^D x = 7\Delta x \\ \Delta_1^E x = \Delta x, & \Delta_2^E x = 2\Delta x, & \Delta_3^E x = 3\Delta x, & \Delta_4^E x = 4\Delta x, & \Delta_5^E x = 6\Delta x \end{cases}$$

For point A, the standard 11-point centered scheme [29] is used with a mesh size of $2\Delta x$. The calculated coefficient are given in Table I.

	FD11A	FD11B	FD11C
a_1	0.87502577558482	0.61534993594014	0.77608591242104
a_2	-0.28944516727589	-0.05177798826851	-0.15880585249465
a_3	0.09231030840505	0.01029785156943	0.01356408535315
a_4	-0.02152267755252	-0.00190780289577	-0.00262508673197
a_5	0.00260486879238	0.00020548792096	0.00037749644344
	FD11D	FD11E	
a_1	0.82482990265298	0.85768936001354	
a_2	-0.22249401437499	-0.26560173861406	
a_3	0.04320809837104	0.07376193338070	
a_4	-0.00210288198432	-0.01244166166264	
a_5	0.00014974870079	0.00033249395384	

Table I. Coefficients of 11-point stencil finite-difference schemes of 4th-order and optimized in wavenumber space. FD11A means finite difference on eleven points at point A.

The dispersion error can be analysed in wavenumber space [32]. The effective wavenumbers resulting from the particular finite-difference schemes at points A, B, C, D and E, as defined by (5), are plotted in Figure 3. The relationship for the scheme used at interior points with spacing Δx is also depicted. Note that at point A (Figure 2), the stencil is that of interior points in the coarse grid with spacing $2\Delta x$. When plotted as a function of $k\Delta x$, the Nyquist criterion yields a limit of $\pi/2$, explaining that the dashed line used for point A ends at $\pi/2$. In Figure 3(a), the deviation from the exact relationship, represented by the median line, indicates the limit of resolvability of the scheme. First, it is worth noting that the curves for the stencils B to E lie in between those of interior points on the fine grid (solid line) and coarse grid (dashed line), respectively. A continuous transition from the coarse to the fine resolution (A to E) is important to reduce spurious reflection due to the grid-size mismatch. The dispersion error is plotted in Figure 3(b) on a logarithmic scale to highlight the limit of resolvability of each scheme. The resolvability is seen to be continuously reduced from

approximately $\pi/2$ ($4\Delta x$ per wavelength) for the fine grid to $\pi/4$ ($4 \times 2\Delta x$ per wavelength) for the coarse grid.
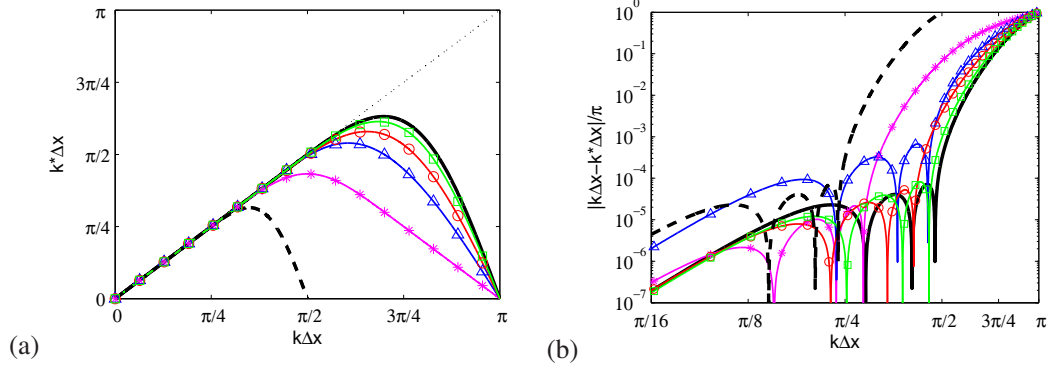

Figure 3. (a) Effective wavenumber $k^*\Delta x$ of the 11-point schemes as function of the reduced wavenumber $k\Delta x$: interior points on the fine grid (——), E (—— □), D (—— ○), C (—— △), B (—— ∗) and A (▬ ▬ ▬) equivalent to interior points on the coarse grid. (b) Dispersion errors represented on a logarithmic scale.

2.3. Spatial filtering

Since a centered finite-difference scheme is systematically   used, the differentiation is not dissipative. That is why a filtering procedure is employed to remove spurious high-frequency oscillations, which can be excited at the location of the interfaces and boundary conditions. An 11-point centered filter of tenth-order [33] is chosen for the two-dimensional laminar cases at moderate Mach numbers treated in the present study. Note that optimized filters would enhance the resolvability and would be beneficial for large-eddy simulations of turbulent flow, where the grid cut-off wavenumber is well inside the broadband energy spectrum [34].

New coefficients have been calculated for 11-point centered filters at the particular points A, B, C, D and E which use the same stencils as the corresponding finite difference schemes (Figure 2). For instance, at point B, a filtered variable is written as

$$f^{\text{filtered}}(x_B) = f(x_B) - \chi D_f(x_B) \quad \text{with} \quad 0 \le \chi \le 1$$

and

$$D_f(x_B) = d_0^B f(x_B) + \sum_{j=1}^{5} d_j^B (f_j^B + f_{-j}^B)$$

where f_j^B and f_{-j}^B are defined by (3). The terms of the Taylor expansion are canceled up to Δx^{10} to obtain the d_j^B coefficients. In Fourier space, the relationship $D_k(\pi) = 1$ is added, yielding the

following system:

$$
\begin{cases}
d_0^B + 2\sum_{j=1}^{5} d_j^B & = & 0 \\
\sum_{j=1}^{5}\left(\dfrac{\Delta_j^B x}{\Delta x}\right)^q d_j^B & = & 0 & 1 \le q \le 4 \\
d_0^B + 2\sum_{j=1}^{5}(-1)^{\left(\frac{\Delta_j^B x}{\Delta x}\right)} d_j^B & = & 1
\end{cases}
$$

where Δ_j^B is given by (4). The calculated coefficient are reported in Table II.

	F11A	F11B	F11C	F11D	F11E
d_0	63/256	1/2	11025/32768	9/32	525/2048
d_1	-105/512	-19845/65536	-1/4	-3675/16384	-27/128
d_2	15/128	2205/32768	735/8192	7/34	945/8192
d_3	-45/1024	-567/32768	-147/16384	-441/16384	-5/128
d_4	5/512	405/131072	9/8192	21/16384	27/4096
d_5	-1/1024	-35/131072	-5/65536	-1/16384	-1/8192

Table II. Coefficients of tenth-order filters for the interface points.

The damping function is obtained by applying a spatial Fourier transform:

$$
D_k\left(k\Delta x\right) = d_0^B + \sum_{j=1}^{5} d_j^B \cos(k\Delta_j^B x) \tag{6}
$$

The transfer functions (6) of the filters at points A, B, C, D and E are compared in Figure 4. The filter at point A is the standard tenth-order filter [33], used for interior points, with a double mesh size. The resolvability limit is progressively increased from point B up to point E. The smooth transition from scheme A to E ensures that disturbances at the block interfaces are minimized. In the following, the filtering procedure is applied every four timesteps with $\chi=0.2$. It has been checked that changing the frequency of filtering or the amplitude coefficient does not change the results [35]. In fact, since the filter activity is restricted to high wavenumbers, well above the wavenumbers of interest, the results are weakly affected by the amplitude of the filtering.

2.4. Multi-dimensional interpolation scheme

The previous paragraphs have detailed the specific treatments developed to deal with the doubling of the mesh size along coincident mesh lines between the fine and coarse grids. Specific treatments must also be applied to deal with mesh lines from the fine grid with no counterpart in the coarse grid. These treatments are described in the context of general curvilinear meshes. The values marked by squares in Figure 2(b), located in the coarse grid, are used to differentiate the fluxes in the interface zone of the fine grid. These values are interpolated from known values at the nodes of the coarse grid, as depicted in Figure 5.

For a Cartesian mesh, values can be interpolated with a directional interpolation technique. DRP optimized coefficients can be computed as proposed by Tam and Kurbatskii [36] for a 7-point
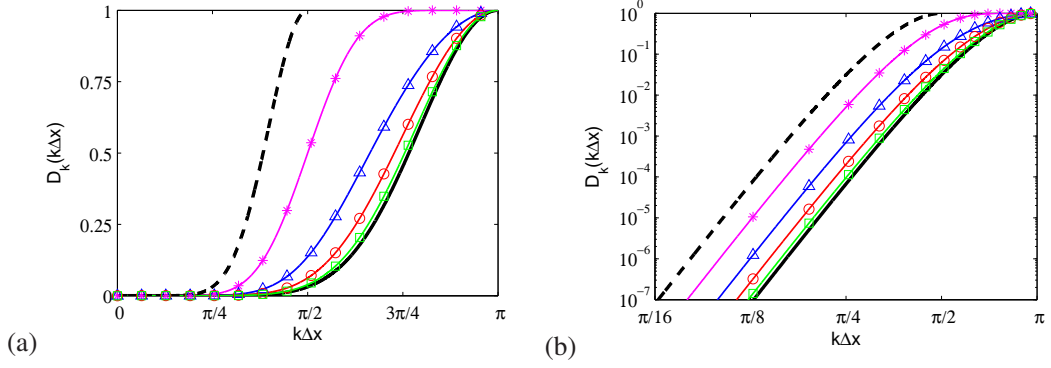
Figure 4. (a) Damping functions of the tenth-order filters at interior points on the fine grid (——), particular point E (——□), D (——○), C (——△), B (——∗) and A (– – –) equivalent to interior points on the coarse grid. (b) Damping functions on a logarithmic scale.
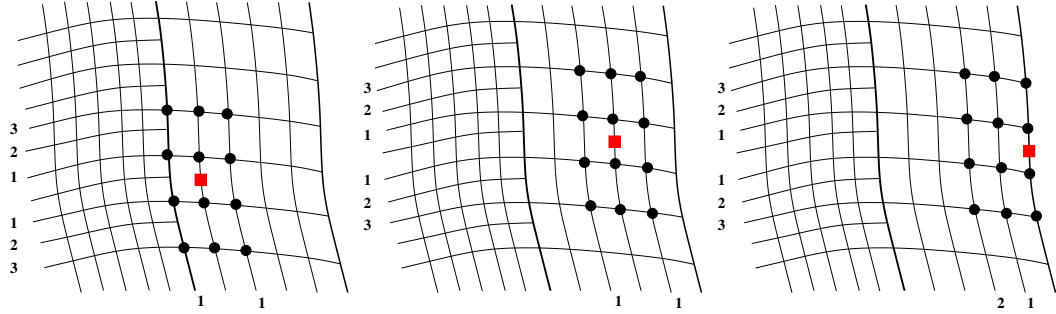

Figure 5. Arrangement of the interpolation stencil (●) for different locations of the interpolated point (■) in the curvilinear physical space.

stencil, and extended by Gloerfelt [37] to 11-point stencil. When the mesh is no longer Cartesian, the data are exchanged in the curvilinear physical space and not in the Cartesian computational space. For that purpose a multi-dimensional interpolation scheme is proposed, taking into account the deformation of the interpolation stencil. For instance, the value at point (x_0, y_0) is interpolated from those of the N neighboring points (x_k, y_k):

$$u(x_0, y_0) = \sum_{k=1}^{N} S_k u(x_k, y_k)$$ (7)

The interpolation coefficients S_k are calculated by minimizing an error in the wavenumber space with constraints on the truncation order [38]. The method is detailed in chapter 13 of the textbook of Tam [21] in the context of overlapping grids. To preserve the high accuracy of the numerical algorithm, a 3×4 point stencil is chosen as depicted in Figure 5. The 12-point stencils allow the calculation of third-order interpolation coefficients optimized in the wavenumber space. The coefficients are computed and stored at the beginning of the simulation for each interpolation point.
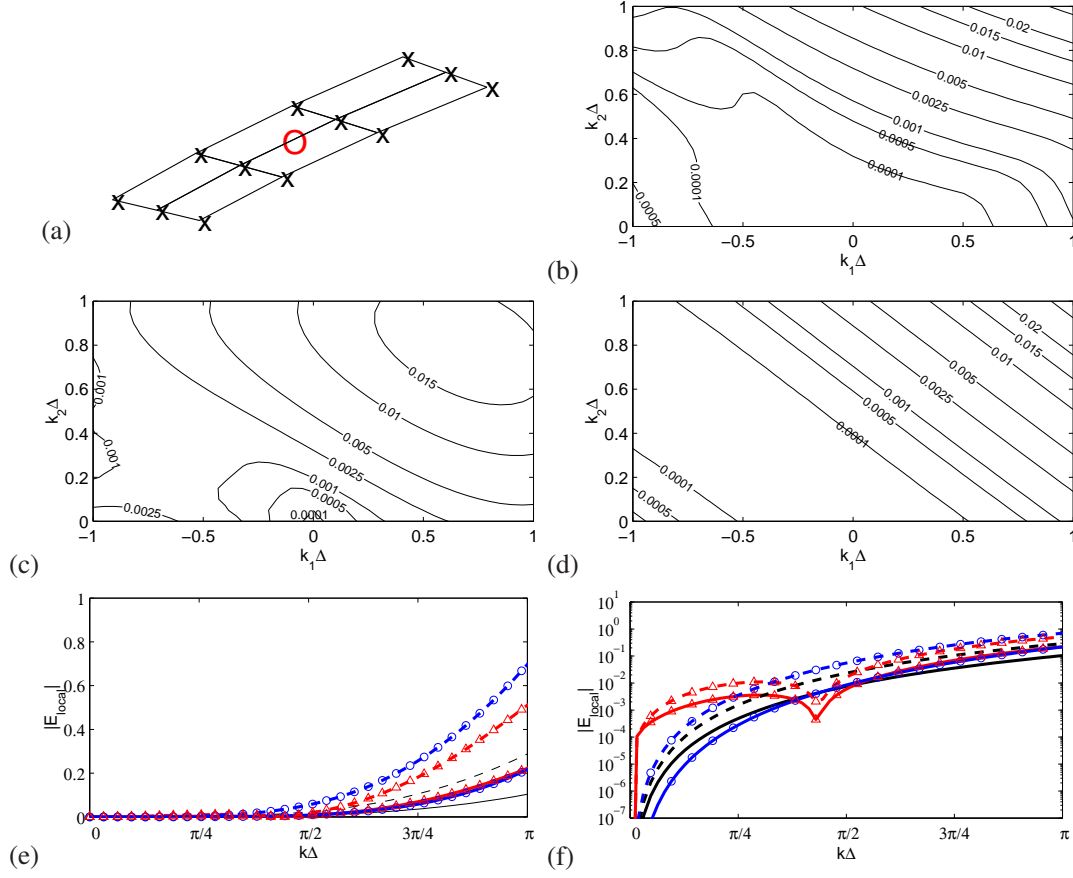
Figure 6. Multidimensional interpolation. (a) View of the interpolation stencil ($\times$) and the interpolated point ($\circ$). Maps of the local interpolation error (8) with coefficients calculated with: (b) order constraints alone; (c) full optimization; (d) combination of order constraints and optimization procedure. Some profiles of the local interpolation error are proposed in (e) and (f) with linear and logarithmic scales, respectively: order constraints alone (b) along $y = 0$ (———$\circ$) and $x = 0$ (— — —$\circ$); full optimization (c) along $y = 0$ (——— $\triangle$) and $x = 0$ (— — — $\triangle$); combination of order constraints and optimization procedure (d) along $y = 0$ (———) and $x = 0$ (— — —). The abscissa wavenumber k in plots (e) and (f) denotes either k_1 or k_2 for horizontal and vertical profiles, respectively.

To better understand the interest of combining order constraints in the sense of Taylor expansions and minimization of an error in the wavenumber space, the local interpolation error, defined as

$$E_{local} = \left| 1 - \sum_{k=1}^{N} S_k e^{\imath(k_1 \Delta x(x_k - x_0)/\Delta x + k_2 \Delta y(y_k - y_0)/\Delta y)} \right| \tag{8}$$

is plotted in Figures 6 and 7 for two representative shapes of the interpolation stencil. The particular stencil arrangements are shown in Figures 6(a) and 7(a). Two-dimensional maps of the error in the reduced wavenumber space are represented by using the coefficients S_k resulting from the order constraints alone (Lagragian polynomials) in Figures 6(b) and 7(b), S_k resulting from the full optimization in the wavenumber space in Figures 6(c) and 7(c) and finally S_k resulting from the combination of order constraints and optimization in Figures 6(d) and 7(d). The length scale Δ, used to form reduced quantities, corresponds to the mean of the $|x_i - x_j|$ and $|y_i - y_j|$ for the stencil. For the stencil of Figure 6, the levels of error are greater for the fully optimized interpolation

shown in Figure 6(c) than for the interpolation resulting from the sole order constraints in Figure 6(b). A quantitative comparison along the lines $x = 0$ and $y = 0$ is proposed in Figure 6(e) and 6(f) on a linear and logarithmic scale, respectively. On the x-axis, the optimization allows a reduction of the error for high wavenumbers $k_1 \Delta > \pi/2$, whereas the error (dashed line with $\triangle$) is greater at low wavenumbers with respect to the interpolation with order constraints ($\circ$), as observed on the logarithmic scale in Figure 6(f). This increase of the error at low wavenumbers when the coefficients are deduced from optimization relationships is also visible along the y-axis (solid lines with $\triangle$ and $\circ$ symbols). The optimized interpolation with added order constraints corresponds to the error map in Figure 6(d), which can be interpreted as a mix between Figures 6(b) and 6(c). The associated error profiles in Figures 6(e) and 6(f) (solid lines without symbols) show that the new interpolation has the lowest errors at high wavenumbers (Fig.6(e)), whereas the low-wavenumber behavior is only slightly degraded with respect to the full order-constraint case. The combination of order constraints and optimization is thus an efficient way to enhance resolvability while preserving low levels of error at low wavenumbers. Its suitability is still more evident for the particular stencil of Figure 7. The high levels of error in Figure 7(b) when only order relationships are used is related to rank deficiencies of the corresponding system. The matrix is close to singular due to the almost alignments in the y-direction. The error map in Figure 7(c) for the full optimization is not sensitive to this kind of singularity. By combining order constraints and optimization in Figure 7(d), the errors are substantially reduced in the x-direction. Adding order constraints is here again beneficial for improving low-wavenumber behavior of an optimized multidimensional interpolation. The better overall resolvability and isotropy of the error distribution are obtained by combining the order constraints and the optimization procedure for the determination of the interpolation coefficients.

3. TIME INTEGRATION SCHEMES

The previous section has described how non conformal mesh doubling are managed. The second essential ingredient of the algorithm is the local time stepping. The CFL condition of an explicit time advancement scheme sets indeed a unique time step dictated by the smallest cell dimension. This leads to a waste of calculation time for every cell where the mesh size is significantly larger than this smallest scale. In the multi-size-mesh multi-time-step strategy, the time step is doubled if there is a corresponding doubling in the mesh size, as illustrated in Figure 8. It can be noted in this figure that five points located in the interface zone belonging to the coarse grid need to be evaluated at intermediate time step $n + 1/2$ to allow the evaluation of derivatives in the fine grid. Runge-Kutta schemes do not allow the marching of the interfaces at time $n + 1/2$ since they include fictitious intermediate stages to compute the numerical solution from time n to time $n + 1$. As suggested in the original method, Adams-Bashforth methods are selected to access the fluxes at intermediate time $n + 1/2$, while preserving low dissipation and dispersion errors compatible with the chosen spatial discretization schemes.
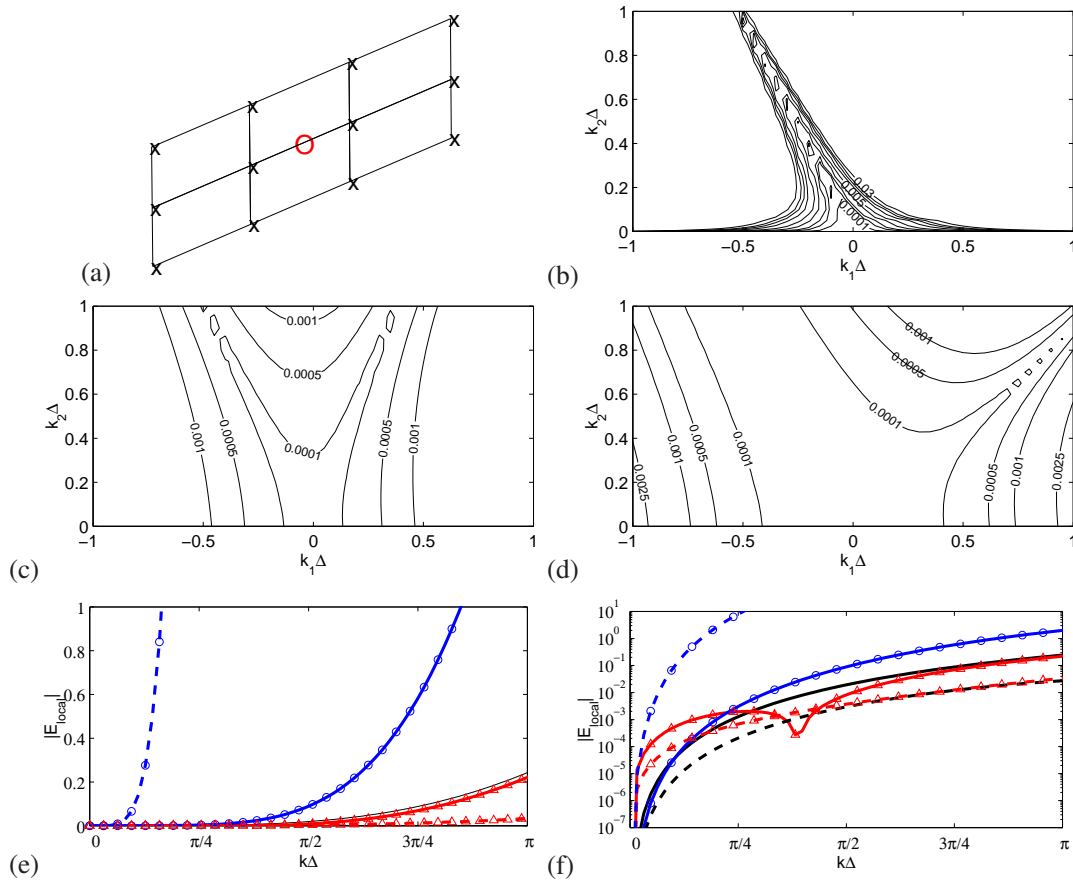
Figure 7. Multidimensional interpolation. Same legend as Figure 6 for the particular stencil in (a).
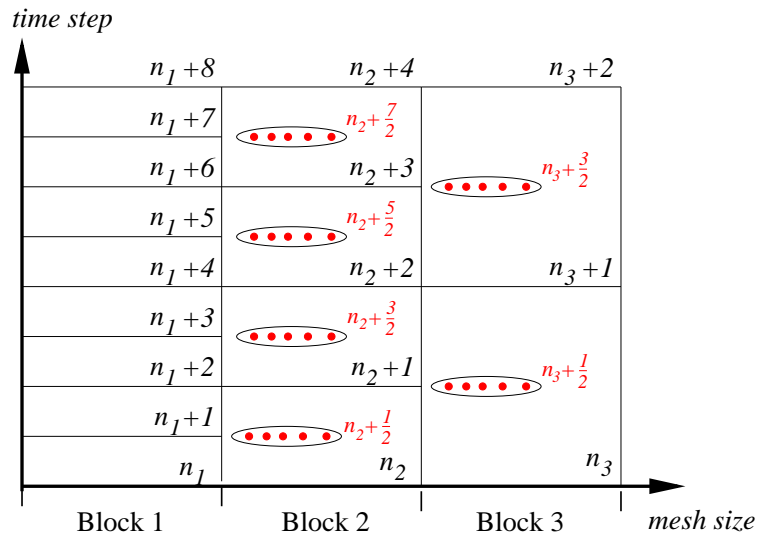

Figure 8. Marching in time with a multi-time-step Adams-Bashforth method: five points, represented by red bullets, need to be advanced at intermediate time steps in the coarse grid interface zone.

3.1. Linear Multistep Methods

The high-order of accuracy is reached by using the informations from previous time steps. A Linear Multistep Method (LMM) with $(p + 1)$ levels is defined as

$$\sum_{j=-1}^{p} a_j \mathbf{U}^{n-j} + \Delta t \sum_{j=-1}^{p} b_j f\left(\mathbf{U}^{n-j}\right) = 0 \,, \tag{9}$$

where a_j and b_j are coefficients, Δt is the advancement timestep, and $a_{-1} = 1$ is fixed. Explicit methods are obtained by choosing $b_{-1} = 0$. For other values of b_{-1}, the algorithm is implicit. When $a_j = 0$ $(j > 0)$, only the fluxes at previous time steps are used. Adams-Moulton schemes constitute the implicit version, while explicit schemes are referred to as Adams-Bashforth methods.

3.1.1. Standard Adams-Bashforth schemes
They are obtained by imposing $a_j = 0$ and $b_{-1} = 0$ in Equation (9). The equation $\partial \mathbf{U}/\partial t = \mathbf{F}(\mathbf{U})$ can be integrated using the formula:

$$\mathbf{U}^{n+1} = \mathbf{U}^n + \Delta t \sum_{j=0}^{p} b_j \left(\frac{\partial \mathbf{U}}{\partial t}\right)^{n-j} \tag{10}$$

where $(p + 1)$ denotes the number of time levels used in the integration formula. To ensure that the scheme remains consistent with the original equation, the coefficients b_j are chosen such that Equation (10) is satisfied to a prescribed order when both sides are expanded in Taylor series:

$$\mathbf{U}^{n+1} = \mathbf{U}^n + \Delta t \frac{\partial \mathbf{U}^n}{\partial t} + \sum_{k=2}^{\infty} \frac{(\Delta t)^k}{k!} \frac{\partial^k \mathbf{U}^n}{\partial t^k}$$

$$\frac{\partial \mathbf{U}}{\partial t}^{n-j} = \frac{\partial \mathbf{U}^n}{\partial t} + \sum_{k=2}^{\infty} \frac{(-j\Delta t)^k}{k!} \frac{\partial^{k+1} \mathbf{U}^n}{\partial t^{k+1}}$$

Identifying each term of the development leads to the following system of equations:

$$\sum_{j=0}^{p} j^m \frac{b_j}{m!} = (-1)^m \frac{1}{(m+1)!} \qquad 0 \le m \le p$$

3.1.2. Optimized Adams-Bashforth schemes
Following Tam and Webb [39], the Laplace transform applied to (10) yields:

$$\omega^* \Delta t = \frac{i(\exp(-i\omega\Delta t) - 1)}{\sum_{j=0}^{p} b_j \exp(ij\omega\Delta t)} \tag{11}$$

where ω^* is the effective angular frequency. The DRP procedure aims at minimizing the dissipation and the dispersion errors in the frequency space. The weighted integral error E is written as

$$E = \int_{\ln(\omega\Delta t)_l}^{\ln(\omega\Delta t)_h} \left(\sigma(Re(\omega^*\Delta t - \omega\Delta t))^2 + (1-\sigma)(Im(\omega^*\Delta t - \omega\Delta t))^2\right) d(\ln(\omega\Delta t))$$

where the upper and lower limits of the integral, $(\omega\Delta t)_l$ and $(\omega\Delta t)_h$, and the weight σ have to be chosen. The σ parameter between 0 and 1 allows to tune the optimization process so as to favor good wave propagation characteristics (real part of ω is emphasized) or good damping characteristics

(imaginary part of ω is emphasized). To derive an optimized scheme of order q with $p + 1$ time-levels ($q \leq p + 1$), the q first relations obtained from Taylor series cancellation up to $\Delta t^{(q-1)}$ must first be satisfied, and $(p + 1 - q)$ extra relations $\partial E / \partial b_j = 0$ ($j = q - 1$ to p) are imposed, to yield $p + 1$ equations with $p + 1$ unknowns b_j. Many coefficients for different number of time levels, scheme order and number of relations imposing $\partial E / \partial b_j = 0$ have been calculated. A 3rd-order, four-level scheme, with $\partial E / \partial b_3 = 0$, has been constructed as a compromise between the formal order, the number of optimized relations and the cost in memory storage induced by the number of levels.

This scheme is entirely defined once the following system is solved:

$$\sum_{j=0}^{p} b_j = 1 \; ; \sum_{j=0}^{p} j b_j = -\frac{1}{2!} \; ; \sum_{j=0}^{p} j^2 \frac{b_j}{2!} = \frac{1}{3!} \; ; \frac{\partial E}{\partial b_3} = 0 \; ,$$

where $(\omega \Delta t)_l = 0$, $(\omega \Delta t)_h = \pi/3$ and $\sigma = 0.45$. The computed coefficients are given in Table III. They are very close to those obtained by Tam and Webb [39], by optimizing with respect to the first coefficient b_0 with a slightly different definition of the error.

Coefficients	Present	Tam and Webb [39]
b_0	2.24778466342984	2.30255809000000
b_1	-2.32668732362284	-2.49100760333333
b_2	1.41002065695617	1.57434093666667
b_3	-0.33111799676317	-0.38589142333333

Table III. Coefficients of the 3rd-order four-level Adams-Bashforth scheme optimized with respect to b_3, and coefficients from Tam and Webb [39].

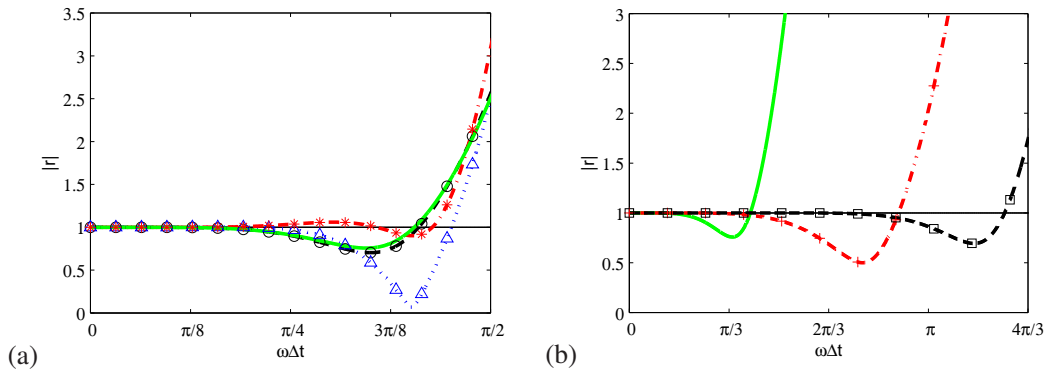### 3.2. Comparison of the explicit time integration schemes

(a)   (b)

Figure 9. Growth factor r. (a) Comparison of different Adams-Bashforth schemes: standard 4th-order scheme (− − − ◦), standard 5th-order scheme (······ △), standard 6th-order scheme (−·−· ∗) and 3rd-order optimized four-level scheme (▬▬). (b) Comparison of the 3rd-order optimized four-level scheme (▬▬) with the standard 4th-order Runge-Kutta (−·−· +) and low-storage 2nd-order optimized Runge-Kutta of Bogey & Bailly [29] with six sub-steps (− − − □).

3.2.1. Stability Stability investigations are realized by studying the growth factor, defined as $g/g_e = re^{-i\varphi}$. For Adams-Bashforth schemes, we have:

$$\frac{g}{g_e} = 1 - i\omega\Delta t \sum_{j=0}^{p} b_j \exp\left(ij\omega\Delta t\right)$$

The module r of the growth factor is plotted in Figure 9(a) for different Adams-Bashforth schemes. The numerical stability is preserved as long as $r < 1$. This limit is slightly enlarged by choosing 5th or 6th-order accuracy. This enlargement of the stability bound is, however, counterbalanced by a further restriction due to the spurious roots when a high order is considered, as will be observed thereafter. The comparison of 3rd-order optimized and standard 4th-order schemes using the same number of time levels indicates that the effect of the wavenumber optimization does not modify significantly the growth factor.

The limit of stability is compared with two Runge-Kutta schemes in Figure 9(b). An Adams-Bashforth scheme yields a lower stability bound. In practical terms, this means that the CFL number used with Adams-Bashforth schemes will be smaller than that of Runge-Kutta schemes. However, since Runge-Kutta schemes include p sub-steps while Adams-Bashforth schemes use a single step, the global calculation cost will remain roughly the same as demonstrated in §3.2.3.
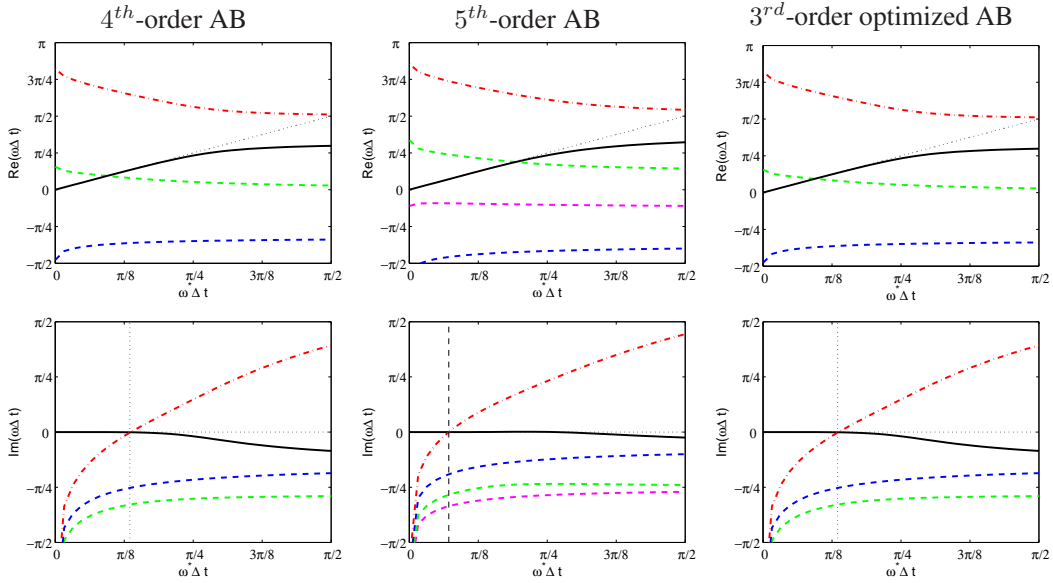

Figure 10. Real part (first row) and imaginary part (second row) of the roots of $\omega\Delta t$ as function of $\omega^*\Delta t$. The solid line represents the physical root superimposed on the exact relationship (thin dotted line) at low frequencies. The dash-dotted line is the spurious root which yields the stability bound (marked by the vertical dashed line in the plots of the imaginary part). The other spurious roots appear as dashed lines.

The analysis of the growth factor g/g_e can be completed by the study of the roots of Equation (11). When multiplying this equation by the denominator of the right-hand side and by $z = e^{i\omega t}$, we get a $(p+1)^{th}$-order polynomial in z:

$$\sum_{j=0}^{p} b_j z^{j+1} + \frac{i}{\omega^*\Delta t}(z-1) = 0$$

For instance a four-level scheme implies the existence of four roots of $\omega\Delta t$ as function of $\omega^*\Delta t$, displayed in Figure 10. Among the roots, the physical one is such that its real part follows the exact relationship for frequencies lower than $\pi/4$. It is represented by the black solid line in Figure 10. The other roots correspond to spurious solutions of (11). The imaginary part of these roots is depicted on the second row of Figure 10. When the imaginary part is negative, a solution is damped in time, whereas a positive imaginary part lead to a solution growing in time and eventually to numerical instability. The effective stability bound thus corresponds to the reduced frequency where the spurious root represented with the red dash-dotted line crosses the positive axis. The same stability bound of 0.425 is noted for the two four-level schemes, namely AB4 of order 4 and ABo3 optimized of order 3. The scheme AB5 (5th-order Adams-Bashforth) is more unstable than AB4 with a stability bound of 0.225.

3.2.2. Dissipation and dispersion errors The real part of the effective angular frequency $\omega^*\Delta t$ is plotted in Figure 11 for the Adams-Bashforth schemes. The dispersion error, plotted on a logarithmic scale in Figure 11(b), is smaller when the order of the standard schemes is increased. However, for frequencies $\omega\Delta t > \pi/4$, we can see in Figure 11(a) a large deviation from the exact relationship for the 5th and 6th-order schemes. The same large deviations near $\pi/3$ are also noticeable for the imaginary part in Figure 12(a) and can compromise the numerical stability. This tendency is intensified for the highest order since Adams-Bashforth schemes can be viewed as fully non-centered finite-difference schemes. Considering the low stability limit as determined by the previous analysis of spurious roots, only frequencies $\omega\Delta t \lesssim \pi/8$ are of interest in practice. In this frequency range, the dispersion and dissipation properties of the four-level optimized scheme are almost similar to the standard 4th-order scheme. Since the DRP optimization is generally efficient to enhance the resolvality limit, this is useless when working only in the low-frequency range $\omega\Delta t \lesssim \pi/8$. We can note in Figure 12(b) that the optimization procedure slightly increases the error of the imaginary part at low frequencies.
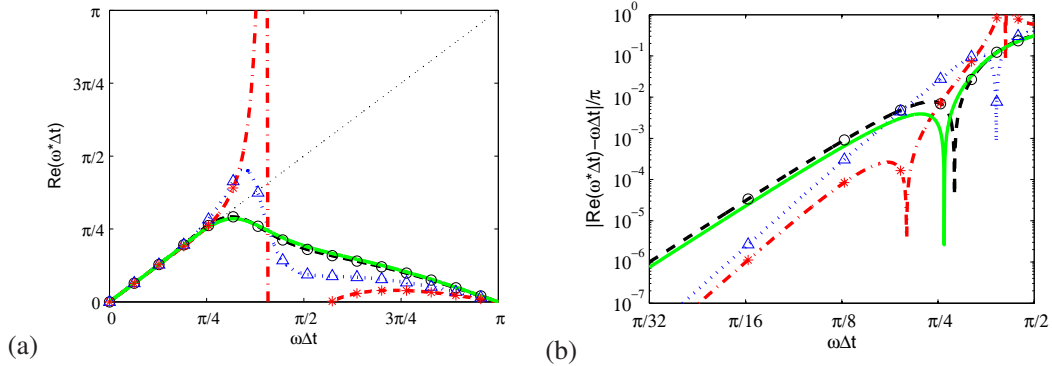

Figure 11. (a) Real part of the effective angular frequency $\omega^*\Delta t$ of Adams-Bashforth schemes as function of the exact angular frequency $\omega\Delta t$: standard 4th-order scheme ($-\ -\ -\ \circ$), standard 5th-order scheme ($\cdots\cdots\ \triangle$), standard 6th-order scheme ($-\cdot-\cdot\ *$), and optimized 3rd-order four-level scheme (———). (b) The errors are represented on a logarithmic scale.

3.2.3. Scalar advection of a wave packet A comparison between Runge-Kutta and Adams-Bashforth schemes is conducted to shed light on the dispersive and dissipative errors induced by
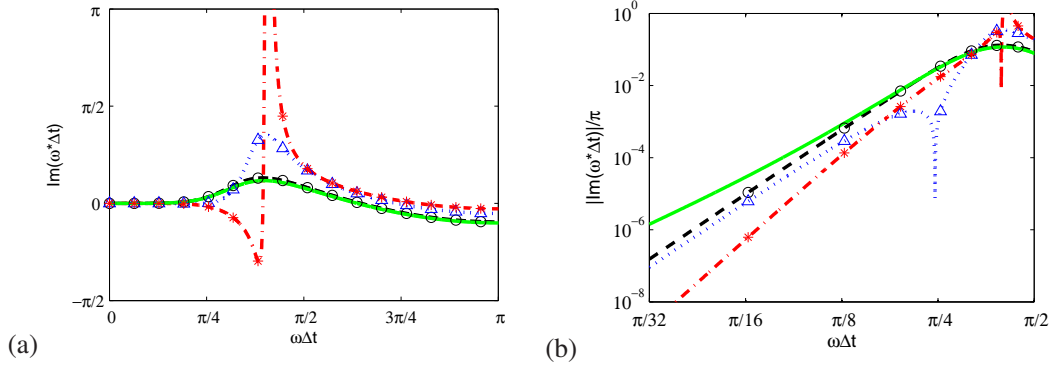
Figure 12. (a) Imaginary part of the effective angular frequency $\omega^* \Delta t$ of Adams-Bashforth schemes as function of the exact angular frequency $\omega \Delta t$: standard 4th-order scheme ($-\ -\ -\ \circ$), standard 5th-order scheme ($\cdots\cdots \triangle$), standard 6th-order scheme ($-\cdot-\cdot \ast$) and optimized 3rd-order four-level scheme (————). (b) The errors are represented on a logarithmic scale.

the time integration procedures. A simple linear scalar advection equation $w_t + aw_x = 0$ is used with $a = 1$. The test case consists in convecting a 1-D wave packet, defined at the initial time by

$$w(x) = \sin\left(\frac{2\pi x}{n_a \Delta x}\right) \exp\left(-\ln 2 \left(\frac{x}{n_b \Delta x}\right)^2\right),$$

where $n_a \Delta x$ is the principal wavelength of the wave packet, $n_b \Delta x$ denotes its Gaussian half width with $\Delta x = 1$. The perturbation is convected over a distance of $800\Delta x$ by enforcing periodic conditions. Two initial configurations are tested here: one with 5 points per wavelength ($n_a = 5$, $n_b = 9$) and the other with 6 points per wavelength ($n_a = 6$, $n_b = 9$). The following integration methods are studied: the low-storage fourth-order Runge-Kutta scheme (RK4), the optimized six-sub-step Runge-Kutta (RK6) of Bogey and Bailly [29], the standard Adams-Bashforth schemes of order 3 (AB3), 4 (AB4) and 5 (AB5) and the third-order four-level optimized scheme (ABo3). The CFL number used for each scheme is given in Table IV and has been chosen to keep the overall cost identical. For example, the Adams-Bashforth schemes imply a single step, and their CFL number is thus divided by six compared with the six-sub-step Runge-Kutta algorithm. The 11-point-stencil DRP finite-difference scheme is used to compute the spatial derivative w_x.

In order to compare the results, a mean quadratic error is computed as

$$L = \sqrt{\frac{\sum_i (w_i - w_{anal})^2}{\sum_i w_{anal}^2}}$$

The results for the different schemes and the different configurations are plotted in Figures 13 ($n_a = 5$, $n_b = 9$) and 14 ($n_a = 6$, $n_b = 9$). It can firstly be noted that the wave packets are hardly resolved by the third-order scheme. The standard RK4 scheme barely improves the results. On the other hand, AB4 and ABo3 schemes provide satisfactory results, which are almost similar, confirming the fact that the optimization has not a significant effect. The optimized scheme ABo3 even yields a quadratic error increased by 6% in the case ($n_a = 6$, $n_b = 9$), compared with the standard AB4 with the same number of levels. No results for the AB5 scheme are given since this scheme is unstable. RK6 globally yields the better results. The errors L are reported in Table IV.
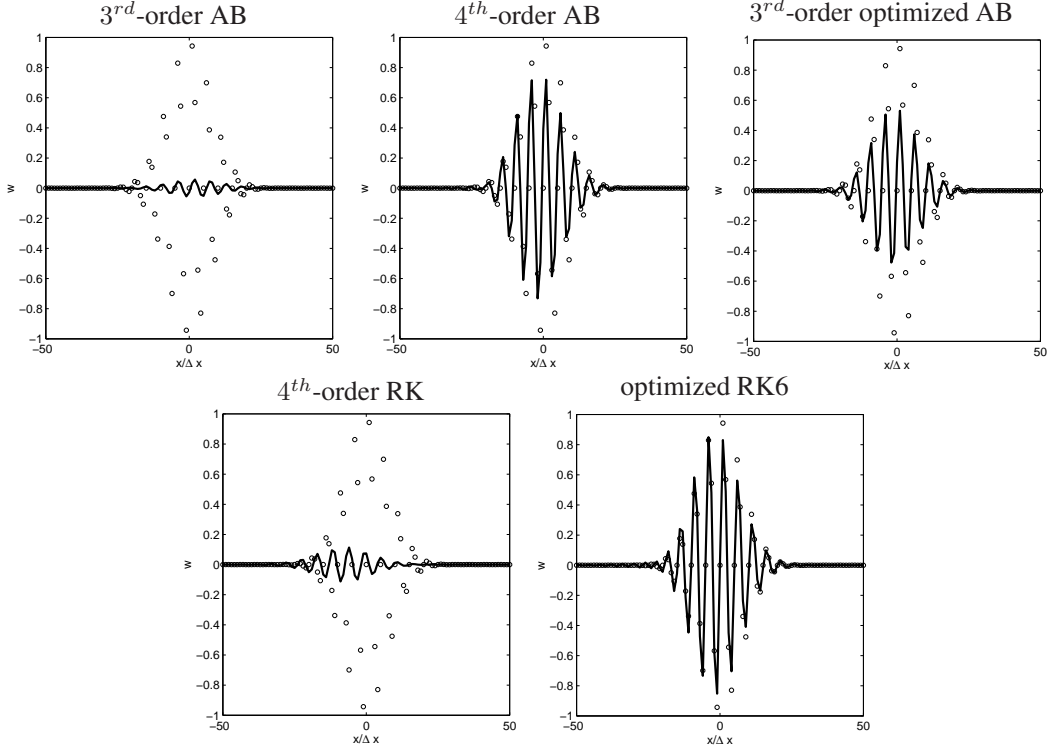
Figure 13. Advection of a wave packet with $n_a = 5$ and $n_b = 9$: numerical (——) and analytical (∘ ∘ ∘) solutions.

The last line ($n_a = 10$, $n_b = 16$) represents a packet discretized by a large number of points. In that case, AB4 can yield a lower error than RK6.

	AB3	AB4	ABo3	RK4	RK6
CFL	1/6	1/6	1/6	2/3	1
($n_a = 5$, $n_b = 9$)	0.964	0.539	0.537	1.064	0.157
($n_a = 6$, $n_b = 9$)	0.809	0.284	0.302	0.985	0.174
($n_a = 10$, $n_b = 16$)	0.236	0.079	0.089	0.104	0.168

Table IV. Advection of a wave packet: mean quadratic errors L, and values of the CFL number.

In summary, the DRP optimization applied to the Adams-Bashforth schemes does not improve significantly their overall resolvability compared to standard versions with the same number of levels. The standard fourth-order Adams-Bashforth has an efficiency comparable with an optimized Runge-Kutta scheme. That is why fourth-order Adams-Bashforth scheme is chosen in the present study.

3.3. Adams-Bashforth scheme at time $n + 1/2$

To advance interfaces in time, the variables need to be calculated at time step $n + 1/2$ since there is no information at this time for the points located on the coarse mesh side (see Figure 8). An equation similar to (10) can be written at time $n + 1/2$:
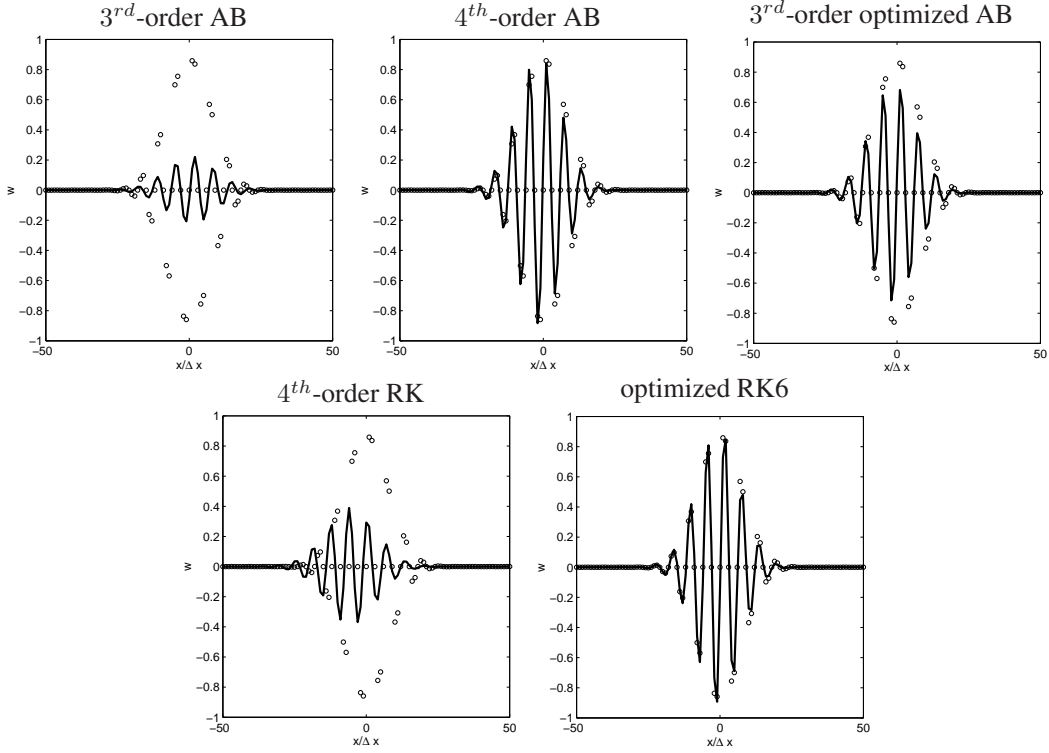
Figure 14. Advection of a wave packet with $n_a = 6$ and $n_b = 9$: numerical (——) and analytical ($\circ \circ \circ$) solutions.

$$\mathbf{U}^{n+\frac{1}{2}} = \mathbf{U}^n + \Delta t \sum_{j=0}^{p} b_j^* \left(\frac{\partial \mathbf{U}}{\partial t} \right)^{n-j} \tag{12}$$

The conditions for p^{th}-order accuracy are readily obtained:

$$\sum_{j=0}^{p} j^m \frac{b_j^*}{m!} = (-1)^m \frac{1}{(m+1)!} \left(\frac{1}{2} \right)^{m+1} \qquad 1 \leq m \leq p$$

Coefficients b_j^* satisfying (12) up to Δt^3 are given in Table V and compared with values provided by Tam and Kurbatskii [20], which are optimized in the wavenumber space with respect to the coefficient b_0^*.

Coefficients	Present	Tam and Kurbatskii [20]
b_0^*	$295/384$	0.773100253426
b_1^*	$-181/384$	-0.485967426944
b_2^*	$101/384$	0.277634093611
b_3^*	$-23/384$	-0.064766920092

Table V. 4th-order four-level Adams-Bashforth scheme at time $n + 1/2$ and coefficients of the 3rd-order optimized scheme of Tam and Kurbatskii [20].
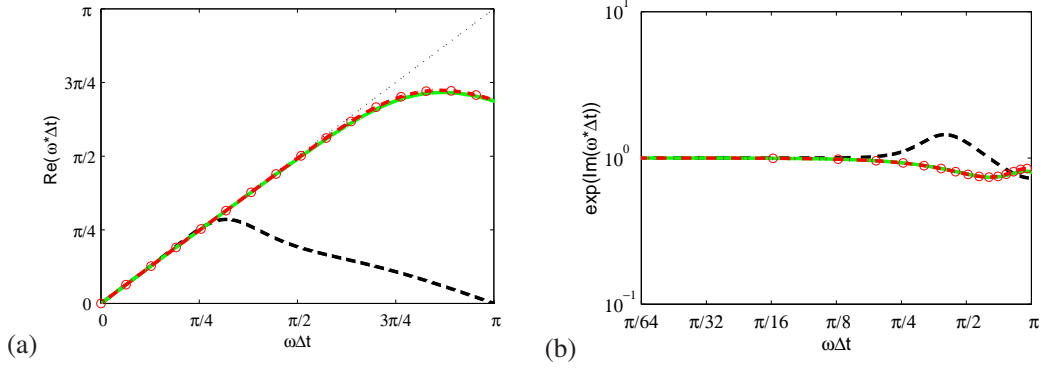
Figure 15. Reduced effective angular frequency $\omega^* \Delta t$ of Adams-Bashforth schemes at time $n + 1/2$ as function of the reduced angular frequency $\omega \Delta t$: (a) real part and (b) imaginary part for the 4th-order scheme (———), optimized scheme of Tam and Kurbatskii [20] (— · — · ○). The 4th-order scheme at time $n + 1$ (— — —) is superimposed.

The effective angular frequency $\omega^* \Delta t$ of these two Adams-Bashforth schemes is plotted in Figure 15, and compared with the 4th-order scheme at time $n + 1$. The schemes for time $n + 1/2$ provide an enlarged resolvability, which is reminiscent of the spatial behavior of staggered schemes [37]. However, the imaginary part of the effective angular frequency is greater for $\omega \Delta t < \pi/4$, as observed in Figure 15. Here again, the optimization of the coefficients in the wavenumber space is not significant and does not justify a reduction of the formal order. That is why the standard 4th-order AB schemes are used in the following for integration at $n + 1$ and $n + 1/2$.

4. GAUSSIAN ACOUSTIC PULSE

The multi-size-mesh, multi-time-step algorithm described in the previous sections has been designed to preserve a low level of dissipative and dispersive errors at the interface between two blocks with different resolution. The test cases hereafter will demonstrate this goal is achieved in practice.

The first test case is a typical wave propagation problem [40]: a two-dimensional acoustic pulse placed in air at rest is propagated over the calculation domain. The initial pressure disturbance has a Gaussian spatial distribution:

$$p - p_\infty = \epsilon \exp\left[-\Lambda\left((x - x_0)^2 + (y - y_0)^2\right)\right] \quad \text{with} \quad \Lambda = \frac{\ln 2}{b^2}$$

where $b = 3$ is the Gaussian half-width and $\epsilon = 100$ Pa is the amplitude. The pulse is centered at $(x_0, y_0) = (0, 0)$. The different quantities are made dimensionless by using Δx of the coarse grid as a length scale, c_∞ as a velocity scale, ρ_∞ as a density scale and $\rho_\infty c_\infty^2$ as a pressure scale. The nondimensional initial amplitude is thus $\epsilon = 7.14 \times 10^{-4}$ and the nondimensional time step is $\Delta t = 0.05$, corresponding to a CFL number of 0.1. The 2-D Euler equations are solved on four different meshes:

- Grid 1 is a uniform 323×161 Cartesian grid with $\Delta x = \Delta y = 0.5$.
- Grid 2 is a 323×161 sinusoidal grid defined by (13) with $\Delta x = \Delta y = 0.5$.

- Grid 3 has one doubling between two Cartesian blocks of size 161×161 and 81×81 with $\Delta x = \Delta y = 0.5$ and $\Delta x = \Delta y = 1$ respectively (plotted in Figure 16(a)).
- Grid 4 has one doubling between two sinusoidal blocks of size 161×161 and 81×81 with $\Delta x = \Delta y = 0.5$ and $\Delta x = \Delta y = 1$ respectively (plotted in Figure 16(b)).

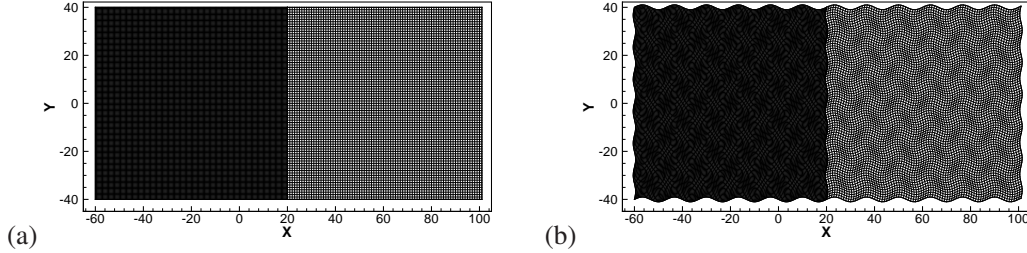(a)   (b)

Figure 16. (a) Configuration with 2 Cartesian blocks and 1 doubling in the mesh size at $x = 20$ (Grid 3); (b) Configuration with 2 curvilinear blocks and 1 doubling at $x = 20$ (Grid 4).

The definition of the sinusoidal meshes is similar to that given by Visbal and Gaitonde [41]:

$$\begin{cases} x(i,j) = x_{min} + \Delta x \left[(i-1) + \sin \left(\frac{3\pi(j-1)\Delta y}{20} \right) \right] \\ y(i,j) = y_{min} + \Delta y \left[(j-1) + 2\sin \left(\frac{3\pi(i-1)\Delta x}{20} \right) \right] \end{cases} \tag{13}$$

where (x_{min}, y_{min}) denote the coordinates of the right bottom corner of the blocks.

The computed results are compared to the analytical solution of this initial value problem [40], given by:

$$p'_{anal}(x,y,t) = \frac{\epsilon}{2\Lambda} \int_0^\infty \exp \left(-\frac{\zeta^2}{4\Lambda} \right) \cos(t\zeta) \, \mathrm{J}_0(\zeta r) \, \zeta \, d\zeta$$

where J_0 is the Bessel function of the first kind and order 0, $r = \sqrt{(x-x_0)^2 + (y-y_0)^2}$. An integral error for the non-uniform grids is defined by integrating in the computational space as

$$\mathcal{E} = \sqrt{\frac{1}{\Omega} \int_0^1 \int_0^1 (p'(\xi,\eta) - p'_{anal})^2 J^{-1} d\xi d\eta} \tag{14}$$

where the Jacobian is defined by (1) and $\Omega = \int_0^1 \int_0^1 J^{-1} d\xi d\eta$. This error is reported in Table VI.

In Figures 17(a) and 18(a), isocontours of the fluctuating pressure are superimposed on their analytical counterparts. In both cases, no distorsion is visible as the pulse goes through the interface thanks notably to the high-order multidimensional interpolation schemes and the specific centered finite difference and filter schemes. The low levels of error are visualized in the right side of Figures 17(b) and 18(b). A slightly greater level of error is observed after the interface since the mesh size is doubled. Small oscillations are noticeable near the location of the doubling in the finer blocks, corresponding to the part of the solution not resolved by the coarse blocks. The maximum errors are visible near the intersection of the radiation boundary conditions and the interfaces at the last instants. The slight increase of the error due to the doubling is reported in Table VI. We also note that the results with the sinusoidal and the Cartesian grids are close, validating the use of the
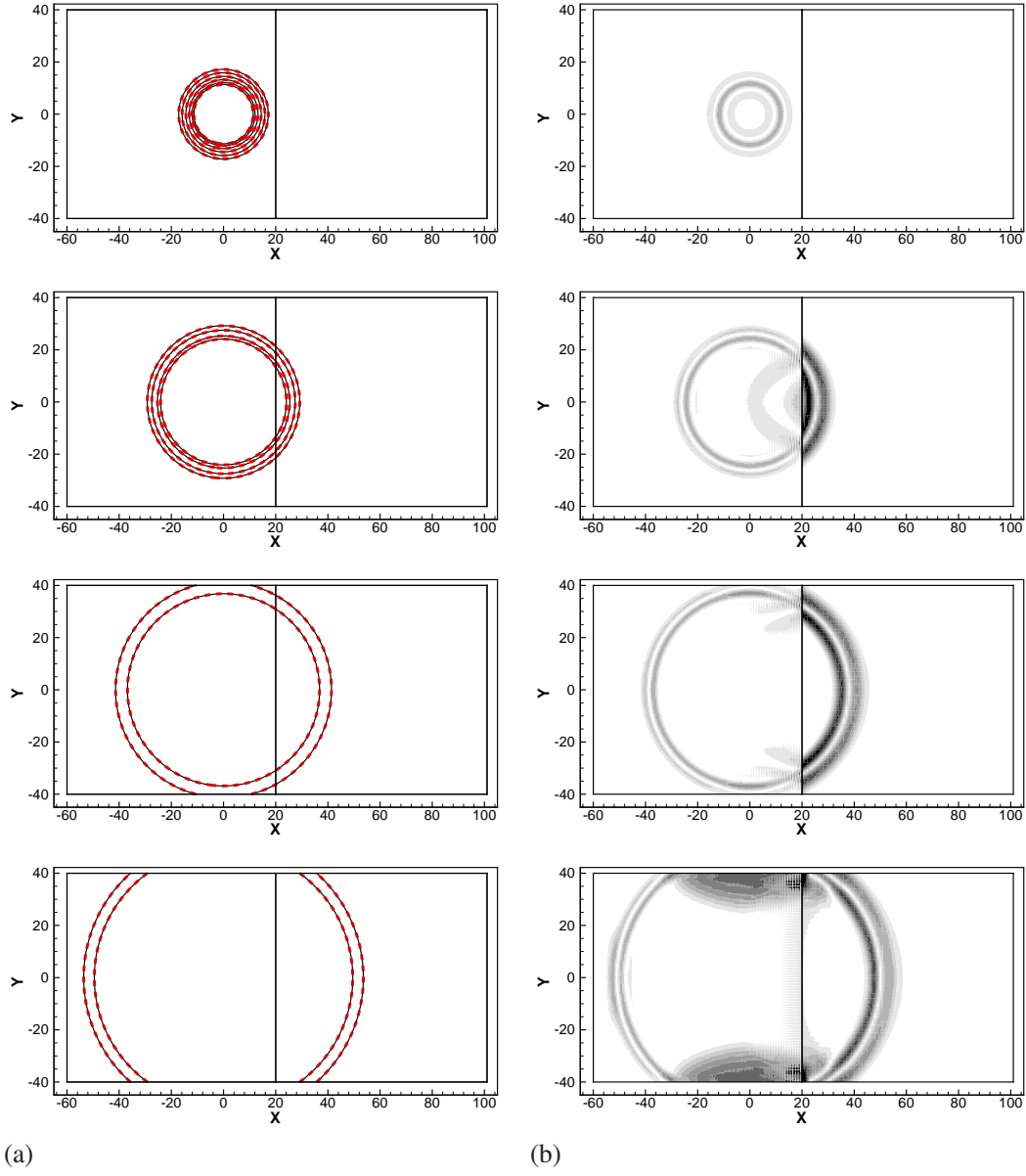
Figure 17. Propagation of a pulse on Grid 3 (Cartesian with doubling) at $t = 12.5,\ 25,\ 37.5,\ 50$. (a) Pressure isocontours between $7{\times}10^{-5}$ and $2.8{\times}10^{-4}$ every $7{\times}10^{-5}$ for the present simulation (——) and the analytical solution (− − −). (b) Error $|p' - p'_{anal}|$ with levels between 0 and $7{\times}10^{-7}$ every $7{\times}10^{-8}$. The interface is represented by the line at $x = 20$.

coordinate mapping and the multidimensional interpolation in the multi-size-mesh multi-time-step algorithm.
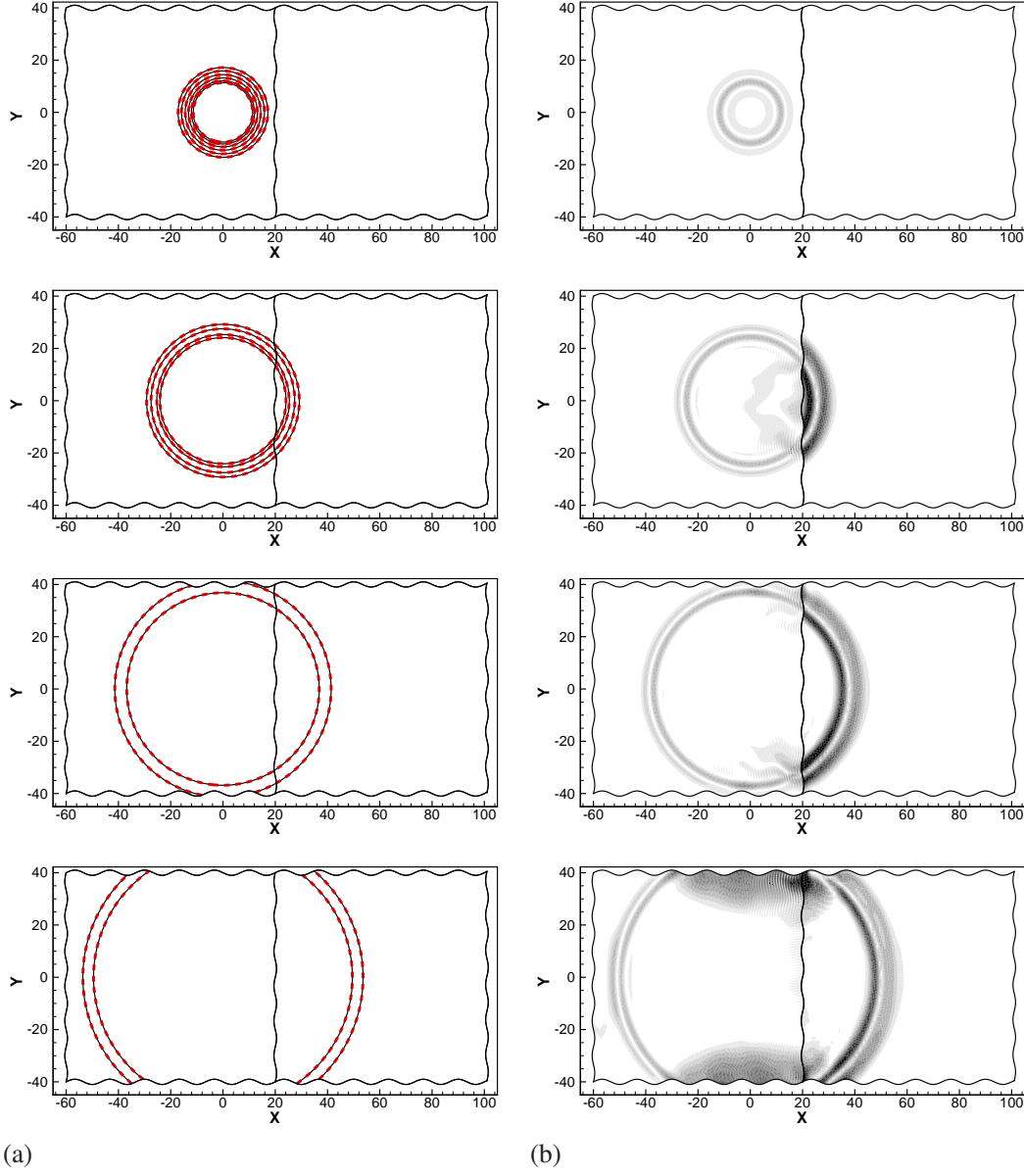
(a)   (b)

Figure 18. Propagation of a pulse on Grid 3 (sinusoidal with doubling) at $t = 12.5, 25, 37.5, 50$. (a) Pressure isocontours between 7×10^{-5} and 2.8×10^{-4} every 7×10^{-5} for the present simulation (———) and the analytical solution ($- - -$). (b) Error $|p' - p'_{anal}|$ with levels between 0 and 7×10^{-7} every 7×10^{-8}. The interface is represented by the line at $x = 20$.

Grids	$t = 12.5$	$t = 25$	$t = 37.5$	$t = 50$
Grid 1 (Cart., w/o doubling)	1.706e-8	2.386e-8	2.962e-8	6.004e-8
Grid 2 (Sin., w/o doubling)	1.705e-8	2.433e-8	3.001e-8	6.010e-8
Grid 3 (Cart., w/ doubling)	2.343e-8	3.734e-8	4.255e-8	8.523e-8
Grid 4 (Sin., w/ doubling)	2.341e-8	3.784e-8	4.419e-8	8.933e-8

Table VI. Gaussian acoustic pulse: nondimensional errors $\mathcal{E}$ defined by (14).
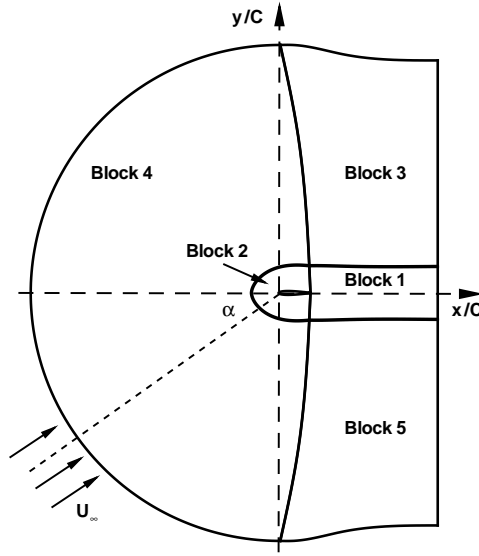
Figure 19. Schematic diagram of the computational domain.

5. LAMINAR TRAILING EDGE NOISE

5.1. Configuration

The simulation of the noise generated by the flow around an airfoil is a good configuration to demonstrate the applicability of the present algorithm. Trailing edge noise comes indeed from the diffraction of the near-field hydrodynamic pressure associated with the vortical motions. It is thus necessary to describe accurately the developing boundary layers on the airfoil body. Large disparities then arise between the fine structures and stiff gradients in the vicinity of the airfoil, and the large wavelengths and weak amplitude of acoustic emissions. The simulation of trailing edge noise is a field of active research [42, 43, 44, 45, 23, 46, 47], and the direct noise computation of a 3-D airfoil at realistic Reynolds numbers is a challenging task [46, 48].

In the present study, a very low Reynolds number configuration is retained to assess the proposed strategy in a two-dimensional case. The laminar flow over a NACA 0012 airfoil at Mach 0.2 and Reynolds 5000 based on the airfoil chord C has been investigated by Mittal and Tezduyar [49], Hatakeyama and Inoue [50] and Ikeda et al. [51]. Two values of the angle of attack $\alpha = 5°$ and $10°$ will be considered in the present study. One doubling in the mesh size is realized at a distance of roughly $0.1C$ from the airfoil surface. This is thus a challenging case insofar as the doubling arises well inside the vortical flow. At the lowest angle of attack of $5°$, the level of acoustic radiation is only few Pascals. It can therefore be checked that the treatment of the doubling does not generate spurious noise that can superimpose on the physical noise radiation. At the higher angle of attack of $10°$, a massive detachment is expected, and the wavelength of the acoustic field increases and can represent several chords. The multi-size mesh multi-time step algorithm is then expected to offer a drastic reduction of the number of points, while preserving the accuracy of the predicted fields.

	$\dfrac{\Delta_{min}}{C}$	$n_\xi \times n_\eta$ w/o doubling	n_{points} w/o doubling	n_{points} w/ doubling	Point saving	$\Delta t(s)$
grid 1	0.0007	1904×496	944 384	323 960	2.92	1.72×10^{-10}
grid 2	0.0014	1700×444	754 800	241 650	3.12	3.45×10^{-10}
grid 3	0.0028	1504×412	619 648	183 676	3.37	6.5×10^{-10}

Table VII. Grid parameters. ξ denotes the coordinate tangential to the airfoil while η is the normal coordinate.

5.2. Numerical setup

CH-type grid systems with 5 blocks have been chosen with one mesh doubling located between blocks 1 and 3, 2 and 4, and 1 and 5, as sketched in Figure 19. The C part of the mesh extends over 35 chords, and the length of the H part is 20 chords in the streamwise direction. In order to check that the domain boundaries are located sufficiently away from the airfoil, a numerical simulation with boundaries pushed away up to $100C$ has also been run [35]. No modifications have been noticed leading to the conclusion that the non-reflecting boundary conditions are sufficiently transparent to avoid any blockage effect, and the present boundary location can be safely used.

(a)   (b)
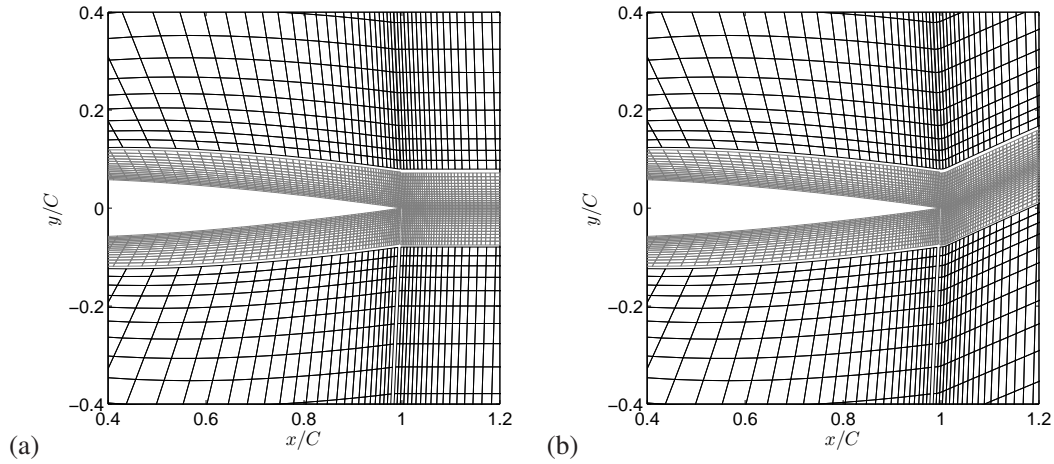
Figure 20. Close-up views of grid 1 near the trailing edge before (——) and after (——) the doubling in mesh size: (a) $\alpha = 5°$ and (b) $\alpha = 10°$. Every fourth mesh points are shown.

The angle of attack is set by imposing the uniform flow parallel to the vector $(\cos\alpha, \sin\alpha)^T$ at the initial time, so the flow in the wake of the airfoil may not be parallel to the x-axis. The mesh has been tilted by $20°$ from the horizontal axis for the simulations with $\alpha = 10°$. Typical close-up views near the trailing edge for the meshes used for $\alpha = 5°$, and $10°$ are presented in Figure 20 (a) and (b), respectively.

On the wall boundary, the no-slip conditions $u = v = 0$ are imposed, with $\partial p/\partial y = 0$. The temperature is calculated with the adiabatic condition. The density can thus be deduced using ideal gas law. The viscous stress terms are evaluated from the interior points by using second-order backward differences. Since an 11-point stencil is used for the interior points, five points need a special treatment near the boundary. The finite-difference stencil for the convective terms is progressively reduced down to the second order, and non-centered 11-point stencils are used for the

	grid 1 $n_\xi \times n_\eta$	grid 2 $n_\xi \times n_\eta$	grid 3 $n_\xi \times n_\eta$
Block 1	672×123	600×83	564×51
Block 2	560×62	500×42	376×26
Block 3	336×217	300×201	282×193
Block 4	280×217	250×201	188×193
Block 5	336×217	300×201	282×193

Table VIII. Details of block configurations for the multi-size-mesh multi-time-step applications.

filtering operation. The values of the coefficients of the non-centered filters can be found in Berland *et al.* [31].

The nonreflecting boundary conditions of Tam and Dong [52] are used at the free boundaries. A radiation condition is applied upstream from the airfoil and an outflow condition downstream of the airfoil. In addition to the outflow boundary condition, a sponge zone is designed to dissipate vortices before they hit the exit plane. The sponge zone combines grid stretching and a Laplacian filter term.

5.3. Grid convergence study

Three levels of grid resolution are designed by doubling the smallest mesh size Δ_{min}/C from Δ_{min}/C=0.0007 to 0.0028. The grid parameters are summarized in Table VII. First, grids without doubling are generated, and will serve as reference. Then, the doubling is imposed, yielding five blocks, whose sizes are given in Table VIII. If we define the point saving as the ratio between the number of points without mesh doubling and the number of points with mesh doubling, a reduction of 2.92 for grid 1, 3.12 for grid 2, and 3.37 for grid 3 is obtained. Since blocks 3, 4 and 5 are advanced every two time-steps, the overall gain in calculation time reaches 4.28, 4.83 and 5.58 for grids 1, 2, and 3 respectively. These theoretical gains are slightly reduced by the extra cost due to the interpolations in the coarse block, but the gains remain significant.

A grid convergence study is conducted with or without doubling for the two selected angles of attack. Figures 21(a) and (b) show the convergence of the mean lift and drag coefficients when refining the mesh without doubling. The coefficients are classically defined as the ratio of the pressure and viscous forces to the upstream dynamic pressure times the airfoil chord, $\rho_\infty U_\infty^2/2 \times C$. The magnitude and frequency of the lift coefficient are rapidly converged for both angles of attack. Only slight differences are visible between grids 1 and 2. The convergence is less rapid for the drag coefficient at α=5°. At α=10°, only small discrepancies can be noted for the coarsest grid 3.

Figures 22(a) and (b) present the convergence results when the mesh doubling at $0.15C$ is used. The overall effect of grid refinement is similar to what was observed for the cases without doubling. At α=5°, the value of the lift obtained with doubling is slightly smaller than without doubling. The values for the mean lift and drag coefficients and for the Strouhal numbers are summarized in Table IX for both angles of attack with or without doubling.

The comparisons between the simulations with or without doubling are presented in Figures 23 and 24 for the finest grid 1. The agreement is very good for the mean pressure coefficient, defined by $c_p = (\overline{p} - p_\infty) / (0.5\rho_\infty U_\infty^2)$, and for the forces on the airfoil. Near-field velocity and pressure fluctuations are thus weakly affected by the mesh doubling, even if it crosses the vortical motions.
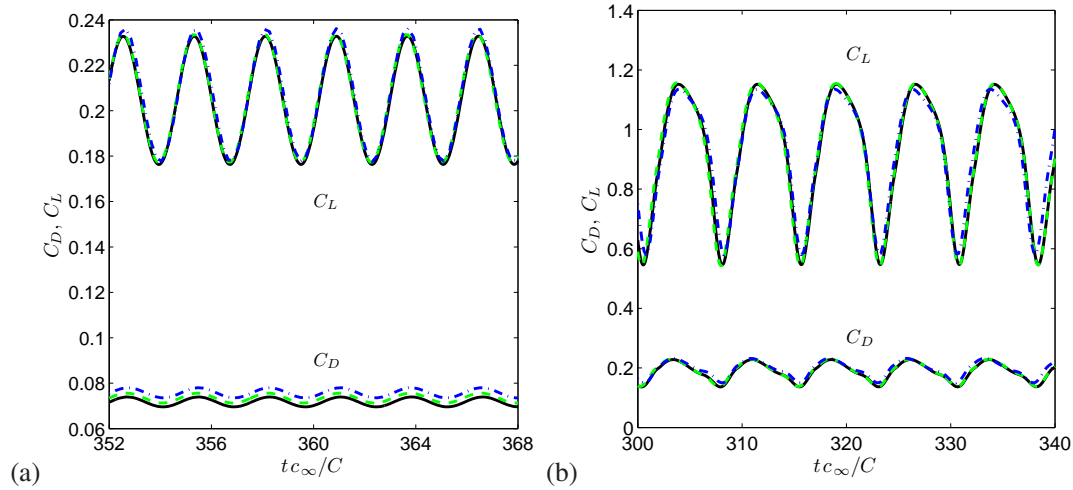
Figure 21. Time evolutions of the lift and drag coefficients for monobloc simulations (without doubling): (a) $\alpha = 5°$; (b) $\alpha = 10°$. Grid 1 (——), grid 2 (− − −), and grid 3 (− · − ·).
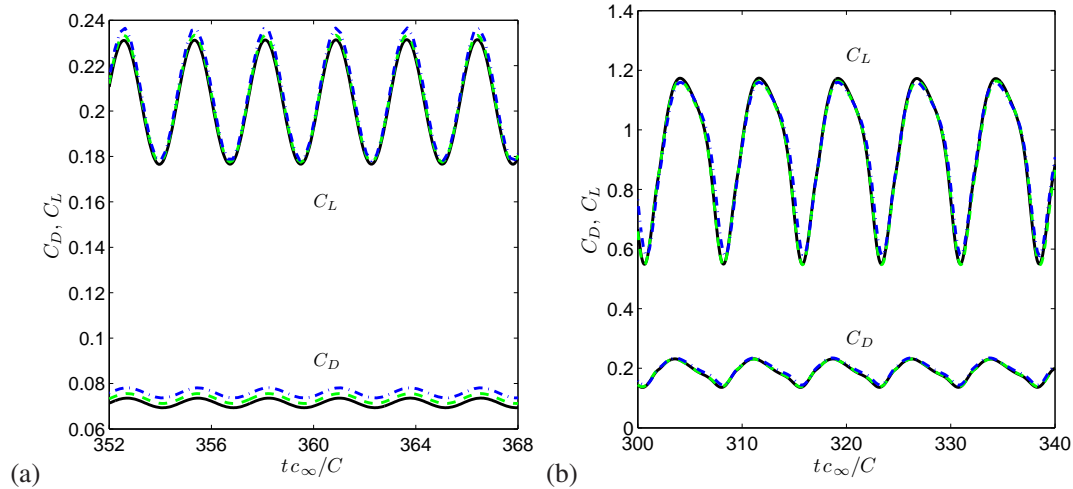

Figure 22. Time evolutions of the lift and drag coefficients for multi-size-mesh multi-time-step simulations: (a) $\alpha = 5°$; (b) $\alpha = 10°$. Grid 1 (——), grid 2 (− − −), grid 3 (− · − ·).

The comparison with the data from the simulation of Hatakeyama and Inoue [50] on their finest grid for $\alpha = 10°$ are also very good.

5.4. Flow and acoustic fields

The results using the space and time doubling strategy are now analysed. Figure 25 shows two snapshots of the vorticity for $\alpha = 5$ and $10°$. For the low angle of attack, the flow looks like an alternate vortex street in the wake of the airfoil. This vortex street resembles the von Kármán street behind a bluff body, such as a cylinder, even if its nature is different. The von Kármán street results indeed from an absolute instability due to the backflow behind the cylinder, whereas the backflow is too weak behind a sharp trailing edge to trigger absolute instability. The vortex shedding
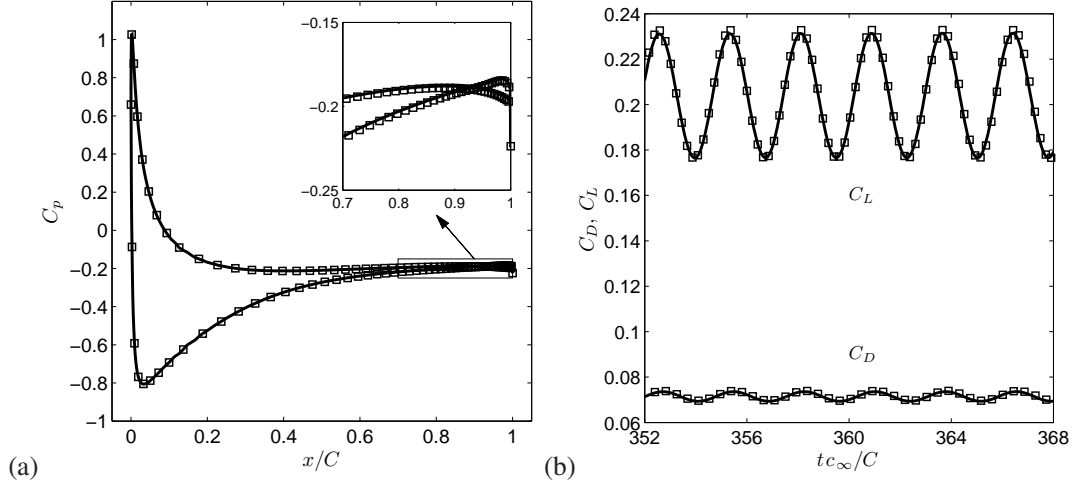
Figure 23. Comparisons of multi-size-mesh multi-time-step simulations (——) and monobloc simulations (□□) at $\alpha = 5°$: (a) mean pressure coefficient; (b) lift and drag histories for grid 1.
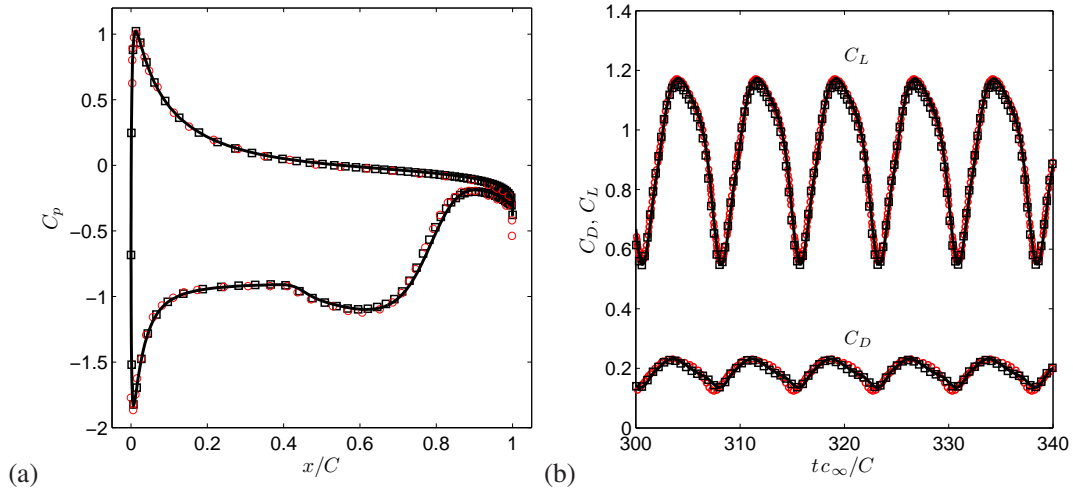

Figure 24. Comparisons of multi-size-mesh multi-time-step simulations (——) and simulations without doubling (□□) at $\alpha = 10°$: (a) mean pressure coefficient; (b) lift and drag histories for grid 1. (∘∘) denote Hatakeyama and Inoue's simulation on their finest grid [50].

$\alpha = 5°$	$\overline{C_L}$	$\overline{C_D}$	St	$\alpha = 10°$	$\overline{C_L}$	$\overline{C_D}$	St
grid 1 w/o doubling	0.204	0.072	1.79	grid 1 w/o doubling	0.926	0.187	0.660
grid 2 w/o doubling	0.205	0.073	1.80	grid 2 w/o doubling	0.911	0.187	0.660
grid 3 w/o doubling	0.208	0.076	1.81	grid 3 w/o doubling	0.936	0.196	0.672
grid 1 w/ doubling	0.204	0.072	1.80	grid 1 w/ doubling	0.934	0.188	0.660
grid 2 w/ doubling	0.206	0.074	1.80	grid 2 w/ doubling	0.929	0.189	0.660
grid 3 w/ doubling	0.208	0.076	1.78	grid 3 w/ doubling	0.944	0.195	0.664
H&I [50]	0.211	0.066	1.81	H&I [50]	0.937	0.183	0.66

(a) (b)

Table IX. Mean lift, mean drag, and Strouhal number St=fC/U_∞ for (a) $\alpha = 5°$ and (b) $\alpha = 10°$. H&I denotes Hatakeyama and Inoue's simulation on their finest grid.

is rather associated with convective Kelvin-Helmholtz-like instabilities of the near-wake velocity profile. The induced acoustic field shown in Figure 27(a) has a dipolar shape. Furthermore, flow and acoustic fields can be characterized by a pure tone, which corresponds to the Strouhal number of the vortex street. Then, for $\alpha > 5°$, the flow becomes asymmetrical; the boundary layer detaches and the separation point gets closer to the leading edge as α increases (Figure 25(b)). For $\alpha > 8°$, a massive detachment appears close to the leading edge. This detachment goes with a quick rolling-up of the whole shear layer, that can be identified in Figure 25(b). This roll impacts the airfoil upstream from the trailing edge and enhances the pressure fluctuations on the solid boundary. As a result, the amplitude and the wavelength of the radiated acoustic field become larger. The formation of strong vortex dipoles in the airfoil wake reveals the limit of the two-dimensional hypothesis. Note that no distorsions of the vorticity isocontours are noticeable when crossing the doubling interface (represented by white lines in Figure 25).
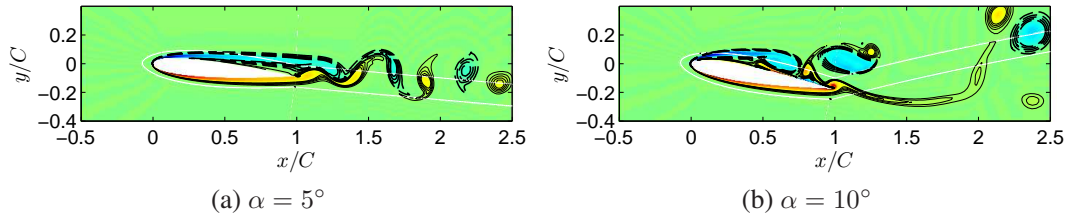

(a) $\alpha = 5°$ (b) $\alpha = 10°$

Figure 25. Vorticity field $\omega = \pm 8 \times 10^5$ s^{-1} with $\Delta\omega_{step} = 1.6 \times 10^4$ s^{-1}, $\omega > 0$ (———), $\omega < 0$ (— — —). The white lines indicate the location of the mesh doubling.
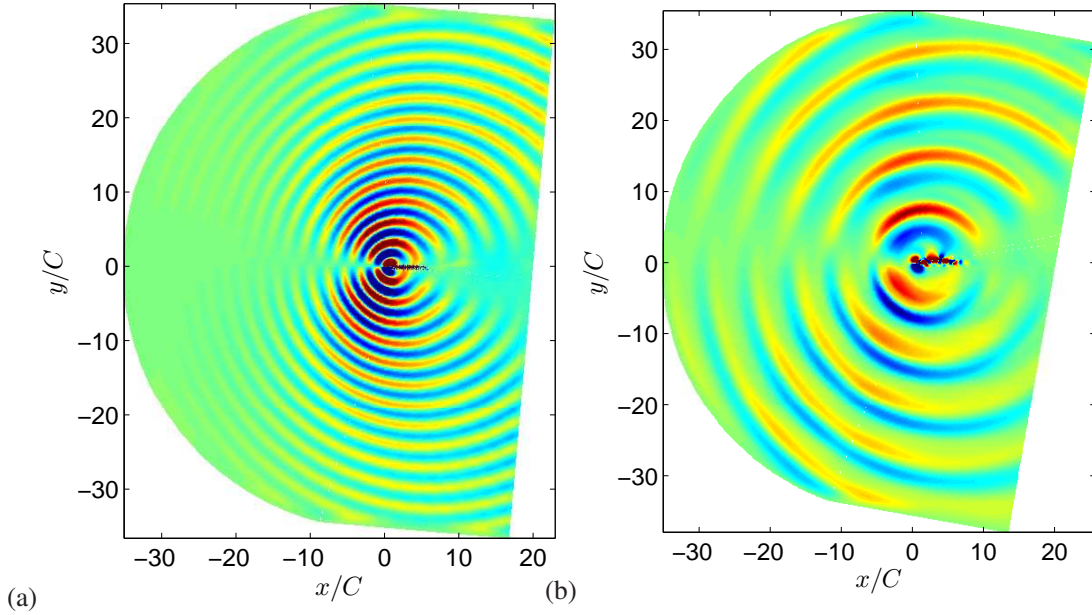

(a)   (b)

Figure 26. Fluctuating pressure $p' = p - \overline{p}$ for: (a) $\alpha = 5°$ (levels ± 10 Pa); (b) $\alpha = 10°$ (levels ± 100 Pa).

Figure 26 shows that the acoustic field is well propagated over the whole computational domain with no spurious reflection due to the free boundaries or the sponge zone. The wavelength of the acoustic field represents several chords of the airfoil. The acoustic source is thus compact, which
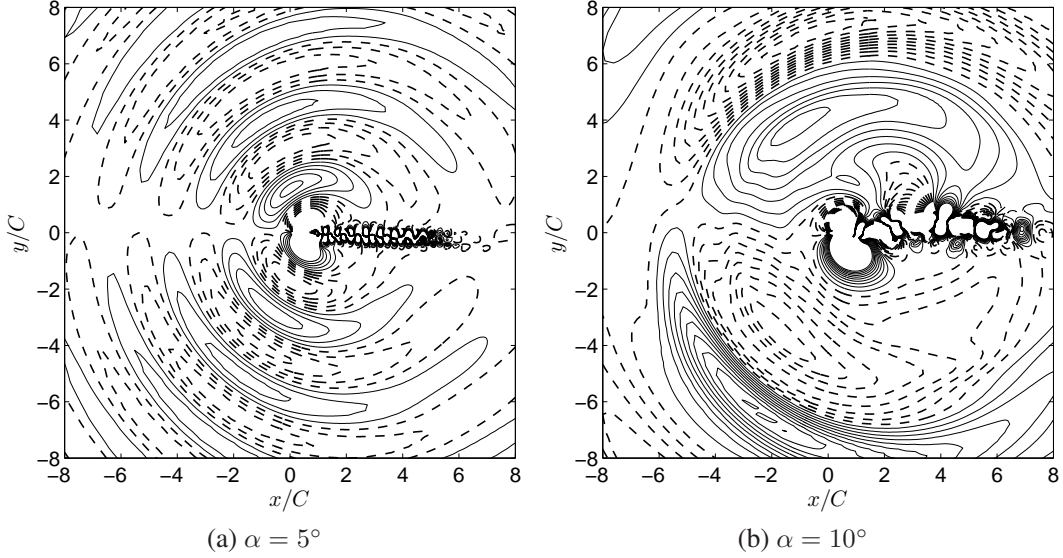
Figure 27. Close-up views of fluctuating pressure $p' > 0$ (———), $p' < 0$ (– – –): (a) ± 20 Pa with $\Delta p'_{step} = 4$ Pa; (b) ± 100 Pa with $\Delta p'_{step} = 10$ Pa.

was expected at the low Mach number considered. The dipolar character is well illustrated by Figure 27, where the phase opposition of the wavefront at the pressure and suction sides are clearly visible.

A quantitative comparison with and without doubling of meshsize is provided in Figure 28, where time histories of pressure fluctuations at different points in the calculation domain are plotted. The sensors are placed at $\Theta = 90° + \alpha$ and $270° + \alpha$ and $R = 30C$. The origin is fixed at $x/C = y/C = 0$ and the angles Θ are measured in the anti-clockwise direction from the horizontal axis. The deformation of the signal for $\alpha = 10°$ reveals the presence of non linear phenomena due to the high-level of acoustic emissions. This results into the emergence of harmonics of the fundamental frequency in the pressure spectrum of Figure 29(b).

The noise levels at the two sensors compare favorably with those obtained in the simulations without doubling, or in Hatakeyama and Inoue's [50] simulations. Since the very small pressure in the far field is more prone to be affected by numerical errors, the very good agreement observed in Figure 28 between the multi-size-mesh, multi-time-step simulation and the simulation without doubling as well as with Hatakeyama and Inoue's simulation demonstrate the quality of the present method as well as its capacity to reproduce a multi scale configuration with a significant reduction of CPU time (here by a factor about 5).

6. TONAL NOISE FROM AN AIRFOIL

In the last example the flow over a NACA0018 airfoil with 6 degrees angle of attack and a Reynolds number $Re_c = 160\,000$ is considered. For moderate Re_c between $50\,000$ and $500\,000$, depending on the exact flow configuration, tonal noise is generated. As shown firstly by Paterson *et al.* [53], the principal tone frequency scales with flow velocity approximately as
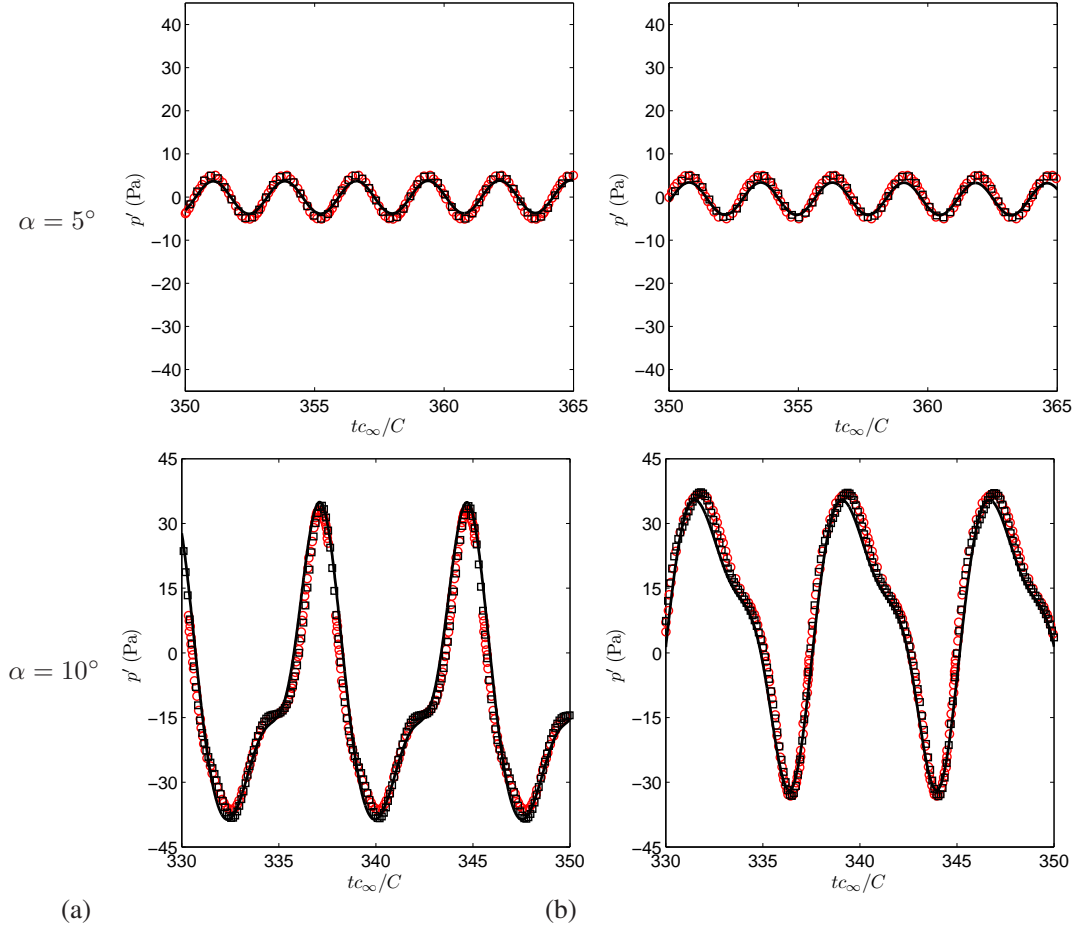
$$f_s = K U_\infty^{1.5} (C\nu)^{-0.5} \tag{15}$$

Figure 28. Time histories of the fluctuating pressure in the far-field at $R = 30C$ and (a) $\Theta = 90° + \alpha$; (b) $\Theta = 270° + \alpha$: multi-size-mesh multi-time-step simulations (———), simulations without doubling ($\square\square$) for grid 1, and Hatakeyama and Inoue's simulation [50] ($\circ\circ$).
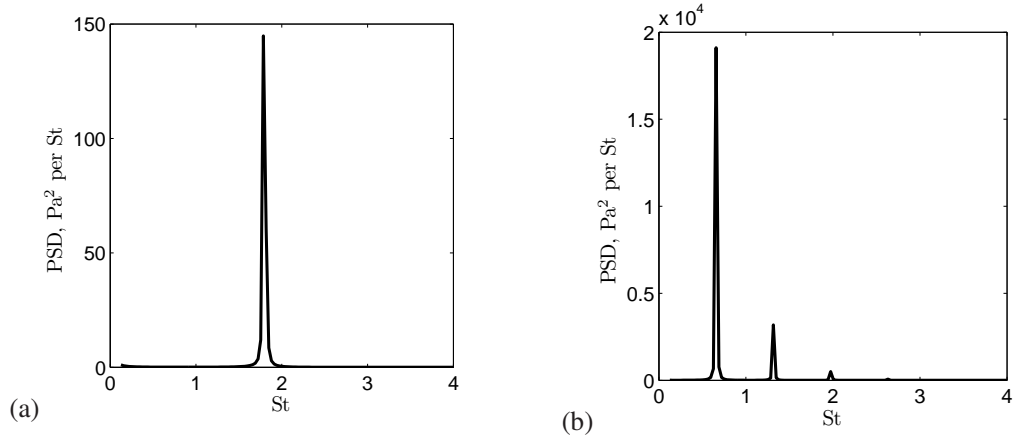

Figure 29. Power spectral densities of the fluctuating pressure at $R = 30C$ and $\Theta = 90° + \alpha$: (a) $\alpha = 5°$, and (b) $\alpha = 10°$ (grid 1).

hereafter referred to as Paterson's formula, where U_∞ is the free-stream velocity, C the chord and ν the kinematic viscosity. Paterson *et al.* [53] found that a constant K=0.011 fits numerous

configurations. This situation corresponds to the case of laminar boundary-layer instability noise in the model of Brooks *et al.* [54]. A necessary condition is indeed that one of the boundary layers developing on airfoil surfaces is laminar or early transitional. In certain configurations, the tone frequency evolves according to a ladder-type dependence on velocity, interpreted as a feedback loop between acoustic waves emitted in the near wake and Tollmien-Schlichting instabilities over airfoil surfaces [55, 56, 57, 58, 59, 60]. As demonstrated recently by Tam and Ju [23] for NACA0012 and zero degree angle of attack conditions, if the boundary layers remain laminar and attached, a single tone is emitted and will follow a Paterson-like formula. The exponent 1.5 in the velocity dependence is in accordance with the most amplified Kelvin-Helmholtz-like instability of the near wake. In constrast, in experiments the environment is sufficiently noisy to trigger instabilities in the boundary layers and the ladder-type behavior results from a synchronisation with these incoming disturbances. The phase relationship between upper and lower sides of the airfoil can sometimes induce a low-frequency desynchronization of the vortex-shedding process in the near wake leading to the appearance of side-band frequencies in the spectra [56, 57, 58, 59, 60].
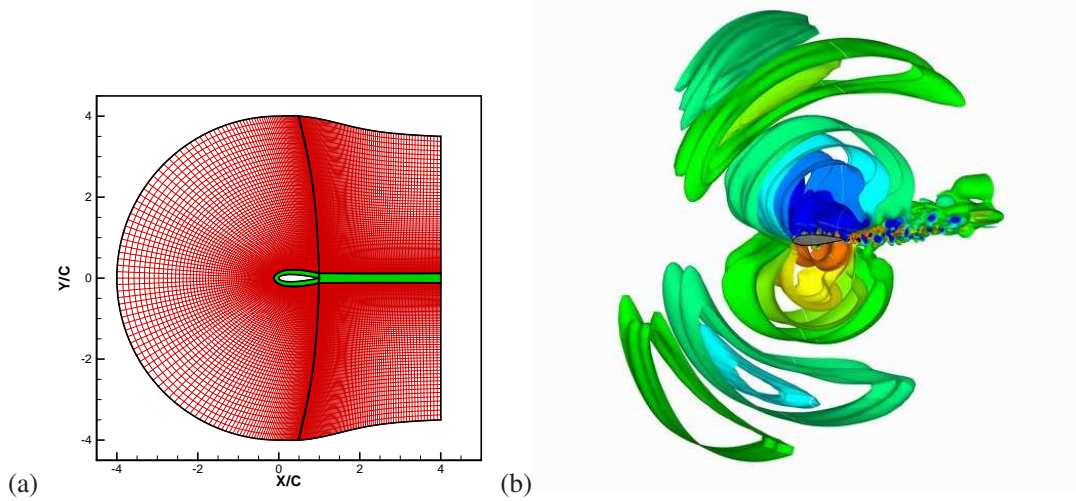

Figure 30. (a) (xy)-cut of the 3-D meshes. The color change $0.15C$ away from the airfoil represents the doubling location. (b) 3-D view of the acoustic field with contour levels between ± 3 Pa.

A three-dimensional version of the present curvilinear multi-size-mesh multi-time-step algorithm is applied on CH grid around a NACA0018 airfoil with a chord C=80 mm, as shown in Figure 30(a). One mesh doubling is imposed at $0.15C$ away from the airfoil resulting in a five blocks configuration as in the previous section (Figure 19). The 3-D mesh is obtained by a simple extrusion in the spanwise direction, that is to say there is no doubling in this direction. The spanwise extent is one C with periodic conditions. Details of the grid parameters are reported in Table X. The use of the multi-size-mesh multi-time-step algorithm allows a reduction by a factor of 2.48 of the number of points. The total saving in calculation time reaches more than 3 thanks to the possibility to double the time step. The simulation is run during a total of 2×10^6 iterations; the first 10^6 iterations are used to establish the flow while the last 10^6 iterations are used to compute the statistics. The simulation costs approximately 200 hours on a NEC SX8 supercomputer.

The free-stream velocity U_∞ is 30 m/s yielding Re_c=160 000. The stream direction is imposed to have an angle of attack of α=6°. Tonal noise is expected for this configuration [61]. Figure 30(b) indeed shows almost two-dimensional acoustic wavefronts regularly emitted near the trailing edge.

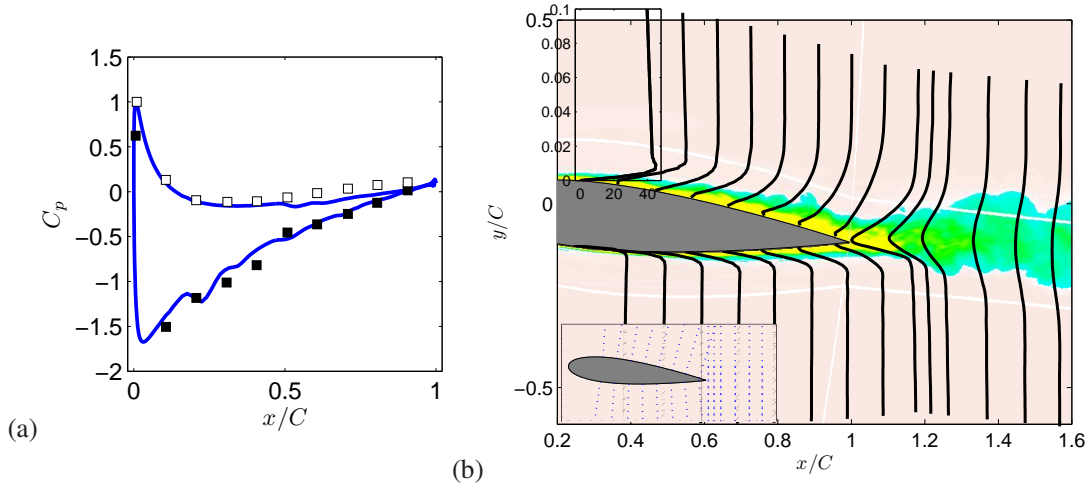|	Δ_{min}/C	$n_\xi \times n_\eta \times n_z$	n_{points}	$\Delta t(s)$
without doubling	0.002	$681 \times 201 \times 41$	5.612×10^6	3.4×10^{-8}
with doubling	0.002	block 1: $190 \times 81 \times 41$		3.4×10^{-8}
	0.002	block 2: $381 \times 41 \times 41$		3.4×10^{-8}
		block 3: $95 \times 95 \times 41$	2.702×10^6	6.8×10^{-8}
		block 4: $161 \times 95 \times 41$		6.8×10^{-8}
		block 5: $95 \times 95 \times 41$		6.8×10^{-8}

Table X. Grid parameters for NACA0018 simulation.

Figure 31. (a) Distribution of mean pressure coefficient (——) compared to experiments of Nakano *et al.* [61] (suction □ and pressure ■ sides). (b) Mean streamwise velocity profiles extracted along the lines shown by blue dotted lines in the insert. The background colormap is the vorticity averaged in the spanwise direction.

First, the time-averaged pressure coefficient from our multi-size-mesh multi-time-step simulation is compared with data measured in a wind tunnel by Nakano *et al.* [61] for a NACA0018 at Re_c=160 000 and α=6° in Figure 31(a). There is a fair agreement between experimental and numerical results providing assurance that the grid resolution is adequate. In particular the pressure distribution is asymmetrical due to the incidence and a large negative value is reached on the suction surface downstream of the leading edge. The pressure level on both sides increases gradually along the chord to form adverse pressure gradients which induce the flow separation. Figure 31(b) shows profiles of the mean streamwise velocity along directions normal to the airfoil surface across the boundary layer and in the near wake. A laminar boundary layer is seen to prevail near the leading edge and it changes to an inflectional profile in the middle of suction surface, which corresponds to the flow separation. This behavior is in qualitative agreement with the measurements of Nakano *et al.* [61]. However, in their experiment, the flow clearly reattaches the suction side, whereas the separation is only weakened in the present simulation. These discrepancies concerning the location of the separation and reattachment points are attributed to the confinement effect in the wind tunnel

(its height of 190 mm represents 2C). On the pressure side, the boundary layer is thinner and the separation appears closer to the trailing edge leading to asymmetrical near-wake profiles. The width of the wake is seen to increase further downstream and the magnitude of the velocity defect is then reduced.
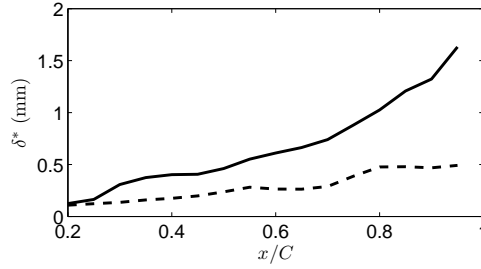

Figure 32. Evolution of the displacement thickness δ^* along the suction (———) and pressure (– – –) sides of the airfoil.

The evolution of the displacement thickness along the chord is shown in Figure 32. Its value rises as the trailing edge is approached due to the flow separation. The sum of the displacement thicknesses on the suction and pressure sides near the trailing edge is found to be 2.1 mm in our simulation in fair agreement with the value of 2 mm measured by Nakano *et al.* [61]. They found that this quantity depends weakly on the angle of attack (between 0 and 15°). Instantaneous views of the vorticity in Figure 33 clearly show the shedding of alternate vortices in the wake. Compared to the low-Reynolds-number case of the previous section or to the perfectly laminar boundary layers in the study of Tam and Ju [23], the regularity of the vortex shedding is here reduced by the disturbances coming from the transitional boundary layers.
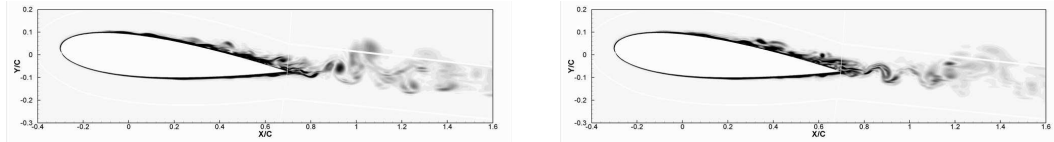

Figure 33. Instantaneous vorticity field $\|\omega\|$ between 0 and $2 \times 10^4 \mathrm{s}^{-1}$ at two instants.

However, the power spectral density (PSD) of velocity fluctuations in the near wake in Figure 34(a) exhibits a well-defined peak at f_s=1590 Hz, showing that there is a preferred frequency for vortex shedding. The noise spectrum at $(x/C,y/C)$=(-1.91,2.36) in Figure 34(b) indicates that the principal tone occurs at the same frequency f_s=1590 Hz, which is in agreement with the fact that the wake instability is the primary source of energy [23]. Note that a higher frequency around 2200 Hz is measured by Nakano *et al.* [61]. Another simulation has been run by including the wind tunnel walls [62, 35] and demonstrated that the confinement significantly modifies the flow leading to a higher vortex-shedding frequency (around 2500 Hz). Furthermore, it was shown that the acoustic field is then contaminated by a Parker mode, *i.e.* a standing acoustic mode due to the rigid walls of the wind tunnel. Nakano *et al.* [61] have reduced the Parker resonance by covering walls by glass wool, but they still observed a higher-frequency tone due to the blockage effects. In the present study, when using the Paterson formula (15) a constant K=0.0106 is obtained in very good agreement with the value 0.011 suggested by Paterson *et al.* [53]. This value is also in good agreement with the

value K=0.0113 obtained by Kingan and Pierce in a similar configuration (NACA0018, C=100 mm, U_∞=30 m/s, α=8°), and K=0.0091 obtained by Tam and Ju [23] based on a linear stability analysis of the wake velocity profile (NACA0012, α=0°, C=100 mm with 0.5% truncation). We consider that the good agreement with the Paterson formula is an indicator that the curvilinear multi-size-mesh multi-time-step strategy do reproduce the essential physics of tonal noise. It can be noticed on the spectra of Figure 34 that secondary peaks appear aside the spectral hump corresponding to the main frequency and could result from a time-to-time desynchronization of the vortex-shedding process in the wake due notably to boundary-layer instabilities on the pressure side. Whether these secondary peaks come from an acoustic feedback loop is, however, beyond the scope of the present study.
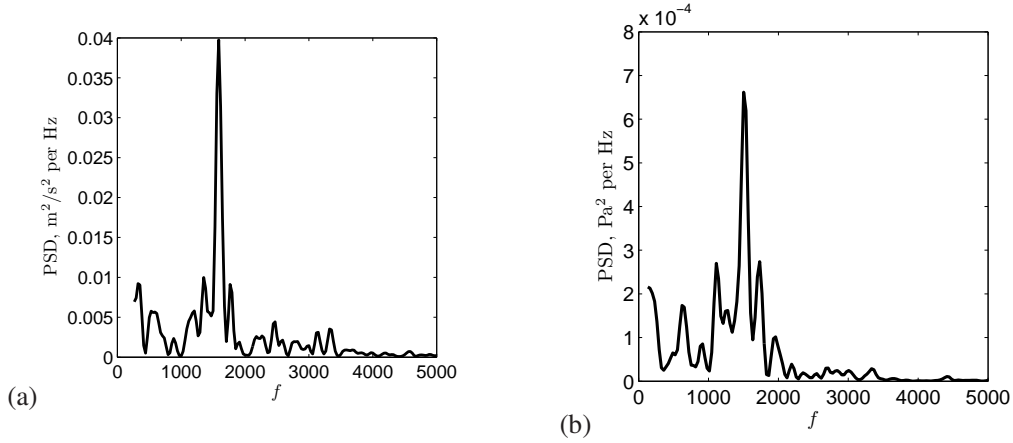

Figure 34. PSD of: (a) fluctuating normal velocity at $(x/C,y/C)$=(1.02,0) and (b) fluctuating pressure at $(x/C,y/C)$=(-1.91,2.36). The spectra are evaluated with Welch method for $10\,000$ samples recorded every $100\Delta t$, giving a sampling frequency of 2.9×10^5 Hz and a resolution $\Delta f \simeq 29$ Hz.

7. CONCLUSION

The multi-size-mesh, multi-time-step algorithm, initially proposed by Tam and Kurbatskii [19], has been extended to large-stencil schemes in general curvilinear grids. Special stencils are used near a mesh doubling to keep centered non dissipative discretization, and to ensure a smooth transition between the coarse and fine grids. The coefficients for finite difference schemes and filters on an 11-point stencil are given. In addition, a multidimensional interpolation procedure optimized in the wavenumber space is used directly in the physical domain. These modifications are validated on some fundamental test cases. The noise generated by the laminar flow over a NACA 0012 airfoil at Reynolds 5000 and Mach 0.2 for two angles of attack represents a challenging implementation of the algorithm. Depending on the angle of attack, the flow corresponds either to an alternate vortex street, or a detached rolling-up from the leading edge. The formation of vortex pairs in the wake of the airfoil reveals the limit of a 2-D assumption. The simulation results for this case have been successfully compared with reference solutions without doubling. The acoustic far field at $30C$ computed using the space and time doubling strategy is almost identical to the far-field computed without doubling, which provides a convincing validation of the method's accuracy. The use of the multi-size mesh multi-time step algorithm reduces drastically the CPU time (by a factor of 5 for

the present 2-D application) by relaxing the constraints imposed by the use of structured meshes and explicit time integration scheme. A three-dimensional implementation has been performed for a NACA0018 at 6° angle of attack and Re_c=160 000. The mean flow features and the frequency of tonal noise are in fair agreement with published studies providing confidence that the numerical strategy developed in the present investigation displays the accuracy needed for studying tonal noise from an airfoil.

ACKNOWLEDGMENTS

REFERENCES

1. COLONIUS, T. & LELE, S.K., 2004, Computational aeroacoustics : progress on nonlinear problems of sound generation, *Progress in Aerospace Sciences*, **40**, p. 345–416.
2. DUMBSER, M., BALSARA, D.S., TORO, E.F. & MUNZ, C.-D., 2008, A unified framework for the construction of one-step finite volume and discontinuous Galerkin schemes on unstructured meshes, *J. Comput. Phys.*, **227**(18), p. 8209–8253.
3. GAITONDE, D.V. & SHANG, J.S., 1997, Optimized compact-difference-based finite-volume schemes for linear wave phenomena, *J. Comput. Phys.*, **138**(2), p. 617–643.
4. KOBAYASHI, M.H., 1999, On a class of Padé finite volume methods, *J. Comput. Phys.*, **156**, p. 137–180.
5. PEREIRA, J.M.C., KOBAYASHI, M.H. & PEREIRA, J.C.F., 2001, A fourth-order-accurate finite compact method for the incompressible Navier-Stokes solutions, *J. Comput. Phys.*, **167**, p. 217–243.
6. LACOR, C., SMIRNOV, S. & BAELMANS, M., 2004, A finite volume formulation of compact central schemes on arbitrary structured grids, *J. Comput. Phys.*, **198**, p. 535–566.
7. POPESCU, M., SHYY, W. & GARBEY, M., 2005, Finite volume treatment of dispersion-relation-preserving and optimized prefactored compact schemes for wave propagation, *J. Comput. Phys.*, **210**, p. 709–729.
8. BERGER, M.J. & OLIGER, J., 1984, Adaptive mesh refinement for hyperbolic partial differential equations, *J. Comput. Phys.*, **53**, p. 484–512.
9. ROGER, M.J. & COLELLA, P., 1989, Local adaptive mesh refinement for shock hydrodynamics, *J. Comput. Phys.*, **82**, p. 64–84.
10. STEINTHORSSON, E., MODIANO, D. & COTELLA, P., 1994, Computations of unsteady viscous compressible flows using Adaptative Mesh Refinement in curvilinear body-fitted grid system, *NASA TM-106704*.
11. KRAVCHENKO, A.G., MOIN, P. & SHARIFF, K, 1999, B-spline method and zonal grids for simulations of complex turbulent flows, *J. Comput. Phys.*, **157**, p. 588–617.
12. BENEK, J., STEGER, J. & DOUGHERTY, F., 1983, A flexible grid embedding technique with application to the Euler equations, *AIAA Paper 83-1944*.
13. STEGER, J.L., DOUGHERTY, F.C. & BENEK, J.A., 1983, A chimera grid scheme, *K. Ghia, U. Ghia (Eds.), Advances in Grid Generation, ASME-FED-Vol. 5, The American Society of Mechanical Engineers*, **5**, p. 55–69.
14. DESQUESNES, G., TERRACOL, M., MANOHA, E. & SAGAUT, P., 2006, On the use of high order overlapping grid method for coupling CFD/CAA, *J. Comput. Phys.*, **220**(1), p. 355–382.
15. SHERER, S.E. & SCOTT, J.N., 2005, High-order compact finite-difference methods on general overset grids, *J. Comput. Phys.*, **210**, p. 459–496.
16. CHICHEPORTICHE, J. & GLOERFELT, X., 2012, Study of interpolation methods for high-accuracy computations on overlapping grids, *Computers and Fluids*, **68**, p. 112–133.
17. DAUDE, F., BERLAND, J., EMMERT, T., LAFON, P., CROUZET, F. & BAILLY, C., 2012, A high-order finite-difference algorithm for direct computation of aerodynamic sound, *Computers and Fluids*, **61**, p. 46–63.

18. MANHART, M., 2004, A zonal grid algorithm for DNS of turbulent boundary layers, *Computers and Fluids*, **33**, p. 435–461.

19. TAM, C.K.W. & KURBATSKII, K.A., 2000, Micro-fluid dynamics and acoustics of resonant liners, *AIAA Journal*, **38**(8), p. 1331–1339.

20. TAM, C.K.W. & KURBATSKII, K.A., 2003, Multi-size mesh multi-time-step dispersion-relation-preserving scheme for multi-scales aeroacoustics problems, *International Journal of Computational Fluid Dynamics*, **17**, p. 119–132.

21. TAM, C.K.W., 2012, *Computational Aeroacoustics: A wave number approach*, Cambridge University Press.

22. YIN, J. & DELFS, J.W., 2001, Simulation of open and ducted-rotor noise using CAA-multidomain method, *Symposium on Developments in Computational Aero and Hydro-Acoustics,* United Kingdom, October 08-11, Symposium Proceedings.

23. TAM, C.K.W. & JU, H., 2012, Aerofoil tones at moderate Reynolds number, *J. Fluid Mech.*, **690**, p. 536–570.

24. ALLAMPALLI, V. & HIXON, R., 2008, Implementation of multi-time step Adams-Bashforth time marching scheme for CAA, *46th AIAA Aerospace Sciences Meeting and Exhibit,* 7-10 January, Reno, Nevada, AIAA Paper 2008-29.

25. LIN, D.K., JIANG, M. & LIN, X.D., 2010, An multi-time-step strategy based on an optimized time interpolation scheme for overset grids, *J. Comput. Acous.*, **18**(2), p. 131–148.

26. LÖRCHER, F., GASSNER, G. & MUNZ, C.-D., 2008, An explicit discontinuous Galerkin scheme with local time-stepping for general unsteady diffusion equations, *J. Comput. Phys.*, **227**(11), p. 5649–5670.

27. LERAT, A. & PEYRET, R., 1974, Noncentered schemes and shock propagation problems, *Computers and Fluids*, **2**, p. 35–52.

28. VINOKUR, M., 1974, Conservation equations of gasdynamics in curvilinear coordinate systems, *J. Comput. Phys.*, **14**(2), p. 105–125.

29. BOGEY, C. & BAILLY, C., 2004, A family of low dispersive and low dissipative explicit schemes for noise computation, *J. Comput. Phys.*, **194**, p. 194–214.

30. BERLAND, J., BOGEY, C. & BAILLY, C., 2008, A study of differentiation errors in large-eddy simulations based on the EDQNM theory, *J. Comput. Phys.*, **227**(18), p. 8314–8340.

31. BERLAND, J., BOGEY, C., MARSDEN, O. & BAILLY, C., 2007, High-order, low dispersive and low dissipative explicit schemes for multiple-scale and boundary problems, *J. Comput. Phys.*, **224**, p. 637–662.

32. VICHNEVETSKY, R. & BOWLES, J.B., 1982, *Fourier analysis of numerical approximations of hyperbolic equations*, SIAM Studies in Applied Mathematics.

33. GAITONDE, D.V. & VISBAL, M.R., 2000, Padé-type higher-order boundary filters for the Navier-Stokes equations, *AIAA Journal*, **38**(11), p. 2103–2112.

34. BERLAND, J., BOGEY, C. & BAILLY, C., 2008, Investigation using statistical closure theory of the influence of the filter shape on scale separation in large-eddy simulation, *J. Turbulence*, **9**(21), p. 1–22.

35. LE GARREC, T. *Simulation direct du bruit de bord de fuite d'un profil par une méthode multi domaines*. PhD thesis, ENSAM, 2008. No ENAM 0021.

36. TAM, C.K.W. & KURBATSKII, K.A., 2000, A wavenumber based extrapolation and interpolation method for use in conjunction with high-order finite difference schemes, *J. Comput. Phys.*, **157**, p. 588–617.

37. GLOERFELT, X., 2006, Aeroacoustic computations of high-Reynolds number cavity flows on staggered grids, in *12th AIAA/CEAS AeroAcoustics Conference, AIAA Paper 2006-2433*, Cambridge, Massachusetts, May.

38. TAM, C.K.W. & HU, F.Q., 2004, An optimized multi-dimensional interpolation scheme for computational aeroacoustics applications using overset grids, *AIAA Paper 2004-2812*.

39. TAM, C.K.W. & WEBB, J.C., 1993, Dispersion-relation-preserving finite difference schemes for computational acoustics, *J. Comput. Phys.*, **107**, p. 262–281.

40. HARDIN, J.C., RISTORCELLI, J.R. & TAM, C.K.W., editors, 1995, *Workshop on benchmark problems in computational aeroacoustics*, ICASE/LaRC. NASA CP - 3300.

41. VISBAL, M.R. & GAITONDE, D.V., 2002, On the use of higher order finite difference schemes on curvilinear and deforming meshes, *J. Comput. Phys.*, **181**, p. 155–185.

42. MANOHA, E., TROFF, B. & SAGAUT, P., 2000, Trailing edge noise prediction using large-eddy simulation and acoustic analogy, *AIAA Journal*, **38**(4), p. 575–583.

43. WANG, M. & MOIN, P., 2000, Computation of trailing-edge flow and noise using large-eddy simulation, *AIAA Journal*, **38**(12), p. 2201–2209.

44. EWERT, R., ZHANG, Q., SCHRÖDER, W. & DELFS, J., 2003, Computation of trailing-edge noise of a 3D lifting airfoil in turbulent subsonic flow, *AIAA Paper 2003-3114*.

45. TERRACOL, M.S., MANOHA, E., HERRERO, C., LABOURASSE, E., REDONNET, S. & SAGAUT, P., 2005, Hybrid method for airframe noise numerical prediction, *Theoret. Comput. Fluid Dynamics*, **19**, p. 197–227.

46. MARSDEN, O., BOGEY, C. & BAILLY, C., 2008, Direct noise computation around a turbulent flow around a zero-incidence airfoil, *AIAA Journal*, **46**(4), p. 874–883.

47. SANDBERG, R.D. & SANDHAM, N.D., 2008, Direct numerical simulation of turbulent flow past a trailing edge and the associated noise generation, *J. Fluid Mech.*, **596**, p. 353–385.

48. LE GARREC, T., GLOERFELT, X. & CORRE, C., 2008, Direct noise computation of trailing edge noise at high Reynolds numbers, *14th AIAA/CEAS AeroAcoustics Conference,* 5-7 May, Vancouver, Canada, AIAA Paper 2008-2914.

49. MITTAL, S. & TEZDUYAR, T.E., 1994, Massively parallel finite element computation of incompressible flows involving fluid-body interactions, *Computer Methods in Applied Mechanics and Engineering*, **112**(1-4), p. 253–282.

50. HATAKEYAMA, N. & INOUE, O., 2006, Direct numerical simulation of noise from an airfoil in a uniform flow, *AIAA Paper 2006-2504*.

51. IKEDA, T., ATOBE, T. & TAKAGI, S., 2012, Direct simulations of trailing-edge noise generation from two-dimensional airfoils at low Reynolds numbers, *J. Sound Vib.*, **331**(3), p. 556–574.

52. TAM, C.K.W. & DONG, Z., 1996, Radiation and outflow boundary conditions for direct computation of acoustic and flow disturbances in a nonuniform mean flow, *J. Comput. Acous.*, **4**(2), p. 175–201.

53. PATERSON, R.W., VOGT, P.G., FINK, M.R. & MUNCH, C.L., 1973, Vortex noise of isolated airfoils, *J. of Aircraft*, **10**(5), p. 296–302.

54. BROOKS, T.F., POPE, D.S. & MARCOLINI, M.A. Airfoil self-noise and prediction. Technical report, NASA Reference Publication 1218, 1989.

55. TAM, C.K.W., 1974, Discrete tones of isolated airfoils, *J. Acoust. Soc. Am.*, **55**(6), p. 1173–1177.

56. ARBEY, H. & BATAILLE, J., 1983, Noise generated by airfoil profiles placed in a uniform laminar flow, *J. Fluid Mech.*, **134**, p. 33–47.

57. DESQUESNES, G., TERRACOL, M. & SAGAUT, P., 2007, Numerical investigation of the tone noise mechanism over a laminar airfoil, *J. Fluid Mech.*, **591**, p. 155–182.

58. KINGAN, M.J. & PEARSE, J.R., 2009, Laminar boundary layer instability noise produced by an aerofoil, *J. Sound Vib.*, **322**, p. 808–828.

59. CHONG, T.P. & JOSEPH, P., 2012, "Ladder" structure in tonal noise generated by laminar flow around an airfoil, *J. Acoust. Soc. Am.*, **131**(6), p. EL461–EL467.

60. ARCONDOULIS, E.J.G., DOOLAN, C.J., BROOKS, L.A. & ZANDER, A.C., 2012, On the generation of airfoil tonal noise at zero angle of attack and low to moderate Reynolds number, *18th AIAA/CEAS AeroAcoustics Conference,* 04-06 June, Colorado Springs, Colorado, AIAA Paper 2012-2060.

61. NAKANO, T., FUJISAWA, N., OGUMA, Y., TAKAGI, Y. & LEE, S., 2007, Experimental study on flow and noise characteristics of NACA0018 airfoil, *J. Wind Eng. Ind. Aerodyn.*, **95**, p. 511531.

62. LE GARREC, T., GLOERFELT, X. & CORRE, C., 2008, A numerical insight into the effect of confinement on trailing edge noise, *Acoustics'08,* June 29-July 4, Paris, France.